



© Copyright by An Nguyen 2018  
All Rights Reserved

APPLICATIONS OF UNMANNED VEHICLES WITH WIRELESS  
SENSOR NETWORKS AND SURVEYING

A Thesis

Presented to

the Faculty of the Department of Electrical and Computer Engineering

University of Houston

in Partial Fulfillment

of the Requirements for the Degree

Master of Science

in Electrical Engineering

by

An Nguyen

December 2018

APPLICATIONS OF UNMANNED VEHICLES WITH WIRELESS  
SENSOR NETWORKS AND SURVEYING

---

An Nguyen

Approved:

---

Chair of the Committee  
Aaron T. Becker, Assistant Professor  
Department of Electrical Engineering

Committee Members:

---

Matthew Franchek, Professor  
Department of Mechanical Engineering

---

Miao Pan, Assistant Professor  
Department of Electrical Engineering

---

Suresh K. Khator, Associate Dean,  
Cullen College of Engineering

---

Badrinath Roysam, Professor and Chair,  
Electrical and Computer Engineering

# Acknowledgements

Thank you to Dr. Aaron Becker, for giving me the opportunity to work on these beautiful projects, with these fascinating people. You are an excellent example of a professor who cares about his student and his teaching as much as his research. I hope the lab continues to grow after I graduate. I hope I graduate.

Thank you to the lab members who came and went during my time here, for putting up with me. Thank you for allowing me to be a lab manager my way, even though it might not have been the most friendly way. I hope you are able to utilize this lab we have built together for a long time.

Thank you to my collaborators, who put up with me when, by my own choice, I worked alone on our collaboration.

Thank you to my parents, Tung Thanh Trinh and Binh Van Nguyen, and my sister, Duong Thuy Nguyen. Mom, you sacrificed your professional and social life for our family. I regret not being able to spend as much time with you when I was in school, I hope that will change soon. Dad, the stories of your struggles showed me that it can work out if I keep going, and with a little bit of luck, or the ancestors' blessing, as you put it. Thank you for giving us a better life, and the opportunity to do what I love. I hope I can be proud of myself as you are of me. I hope I give you guys less headache. Duong, thank you for showing me that you don't have to be successful in school to be successful in life. I wish you and Juan to be happy and fulfilled the rest of your life. I am very grateful that you decide to share that happiness with me.

APPLICATIONS OF UNMANNED VEHICLES WITH WIRELESS  
SENSOR NETWORKS AND SURVEYING

A Thesis

Presented to

the Faculty of the Department of Electrical and Computer Engineering

University of Houston

in Partial Fulfillment

of the Requirements for the Degree

Master of Science

in Electrical Engineering

by

An Nguyen

December 2018

# Abstract

An unmanned vehicle, such as a flying multi-copter, an unmanned rover, a remote-controlled boat, can be used to cover a large area of land, to perform repetitive, tedious yet strenuous tasks for people. We can have an unmanned aerial vehicle (UAV) distribute a network of seismic microphone, used during seismic surveying, in treacherous terrain, free of heavy signal wiring, without risking injury to human workers. A UAV can sweep a large area with a mosquito-zapping net, destructively sampling mosquito population in the area, giving entomology researcher better data about their distribution and behavior through time and space. An unmanned boat, or a UAV, can distribute a drifting wireless sensor network (WSN) into a body of water. The same, or several unmanned vehicles, can then monitor, recharge and finally recollect them. The following thesis presents hardware for all of the above applications, as well as software and algorithms for the unmanned vehicles, and sensor nodes.

# Table of Contents

<b>Acknowledgements</b>	<b>v</b>
<b>Abstract</b>	<b>vii</b>
<b>Table of Contents</b>	<b>viii</b>
<b>List of Figures</b>	<b>xi</b>
<b>List of Tables</b>	<b>xiv</b>
<b>1 Introduction</b>	<b>1</b>
1.1 Autonomous unmanned vehicles . . . . .	1
1.2 Seismic AUV . . . . .	1
1.3 Mosquito AUV . . . . .	3
1.4 Drifting sensors . . . . .	5
<b>2 UAV deploying SeismicDarts</b>	<b>7</b>
2.1 Related Work . . . . .	7
2.1.1 Overview of seismic sensing theory . . . . .	8
2.1.2 Related work . . . . .	10
2.2 SeismicDarts . . . . .	10
2.2.1 Experiments . . . . .	11
2.2.2 SeismicDart deployment and retrieval . . . . .	15

2.3	SeismicSpider . . . . .	16
2.3.1	Shot gather comparison . . . . .	17
2.3.2	Deploying and retrieving the SeismicSpider . . . . .	18
2.4	Deployment Unit (UAV) . . . . .	19
2.4.1	Autonomous drop demonstration and accuracy . . . . .	20
2.4.2	Height vs. penetration depth . . . . .	21
2.4.3	Robustness . . . . .	22
2.5	Comparision . . . . .	23
2.5.1	Ballistic deployment . . . . .	23
2.5.2	Simulation studies . . . . .	25
2.6	Conclusion . . . . .	27
<b>3</b>	<b>UAV surveying mosquitoes</b>	<b>29</b>
3.1	Overview and related work . . . . .	29
3.2	Hardware design . . . . .	31
3.2.1	The UAV . . . . .	31
3.2.2	Screen design . . . . .	31
3.2.3	Screen location . . . . .	32
3.2.4	Wind tunnel verification of net angle . . . . .	34
3.2.5	Data logger . . . . .	35
3.2.6	Energy budget . . . . .	36
3.3	Path planning . . . . .	38
3.3.1	Modelling mosquito density . . . . .	38

3.3.2	Turn Cost . . . . .	38
3.4	Experiments . . . . .	39
3.5	Conclusion and future work . . . . .	43
<b>4</b>	<b>Drifting sensors</b>	<b>44</b>
4.1	Design . . . . .	44
4.1.1	Hardware . . . . .	44
4.1.2	Software . . . . .	46
4.2	Depth sensor . . . . .	47
4.2.1	Overview . . . . .	47
4.2.2	Testing . . . . .	49
4.3	Conclusion . . . . .	53
<b>5</b>	<b>Conclusion</b>	<b>55</b>
	<b>References</b>	<b>56</b>

# List of Figures

1.1	The heterogeneous sensor system presented in chapter 2: wireless SeismicDarts and a SeismicSpider, both designed for UAV deployment. . . . .	2
1.2	A hexacopter UAV carrying a 48 cm × 61 cm rectangular bug-zapping screen. . . . .	4
1.3	Driftnode Overview . . . . .	5
2.1	Comparing state-of-the-art seismic survey sensors. a) A traditional cabled system connects geophones. b) Autonomous nodal systems. . . . .	9
2.2	Components of the SeismicDart sensor: a lawn Jart™ fin, particle.io Photon™ micro-controller, 3D printed protective casing, and a geophone. . . . .	11
2.3	Drop height vs. penetration depth in seven soil types. Drops were performed autonomously and each data point represents 12 trials. Increasing the drop height increased the penetration depth for all seven soil types. . . . .	13
2.4	Drop height vs. angle of deviation in seven soil types Drops were performed autonomously and each data point represents 12 trials Increasing the drop height reduced the angle of deviation for all seven soil types. . . . .	13
2.5	Raw voltage data from shot gather comparison of four traditional geophones and four autonomously dropped SeismicDart sensors. . . . .	15
2.6	SeismicDart retrieval and redeployment. See video attachment. . . . .	16
2.7	The SeismicSpider is a six-legged mobile robot where geophones replace three legs It is drone deployable, can sense and record seismic data, and can move to desired locations, including terrain the SeismicDart cannot access. . . . .	17

2.8	Shot gather comparison of traditional geophones vs. SeismicSpider. . . .	18
2.9	SeismicSpider retrieval and redeployment. See video attachment. . . . .	19
2.10	Deployment system for dropping SeismicDarts from the UAV. Pictured design holds four darts, but can be scaled according to the UAV's carrying capacity. . . . .	20
2.11	a) First set of darts with reference axes. b) Third dart set. . . . .	21
2.12	Targeting accuracy. Circles show landing locations of 24 darts, each commanded to drop at the same GPS location. The mean position is marked by a diamond, ellipses show $\sigma$ and $2\sigma$ covariance. . . . .	22
2.13	A pneumatic launcher for SeismicDarts. Ballistic dart deployment has limited usefulness because the incident angle is equal to the firing angle. .	23
2.14	Screenshots of simulations to estimate time take by different team surveying $100\text{ m} \times 100\text{ m}$ grid: a) only SeismicSpiders b) SeismicDarts and deployment system c) heterogeneous system d) human workers. . . . .	24
2.15	Survey time for a $1\text{ km} \times 10\text{ km}$ region for different numbers of UAVs. . .	25
2.16	Survey time for different sensor ratios. The total number of sensors $\{5000, 3000\}$ were kept constant. Ten darts were provided for each UAV. . . . .	26
3.1	Propwash pushes incoming mosquitoes downwards, and the UAV clears a volume $h_m d_s v_f$ each second. Circles show two mosquitoes at equal time intervals relative to the UAV. . . . .	33
3.2	The volume cleared by a UAV is a function of screen angle $\theta$ and forward velocity $v_f$ . Dotted line shows the optimal angle given in (3.4) . . . . .	35
3.3	Frames from wind tunnel test with free-flying UAV at 3 m/s windspeed with smoke for streaklines. Each black square is 25.4 mm in width. . . . .	36

3.4	Current, voltage, and power traces for five <i>Culex quinquefasciatus</i> mosquitoes as each contacts the bug-zapping screen at $t = 0$ . Contact causes a brief short that recovers in 160 ms. . . . .	37
3.5	Mosquito hunting drone . . . . .	39
3.6	Fountain . . . . .	40
3.7	The UAV's path for flight 3 is in red. Strikes collected along this path are represented by yellow dots. . . . .	41
3.8	Density map showing mosquito distribution on the field, overlaid by flight path 4 in white. . . . .	42
3.9	The UAV and screen during a flight trial near the ocean. . . . .	42
4.1	Driftnode . . . . .	44
4.2	Driftnode . . . . .	47
4.3	Various range finder . . . . .	48
4.4	MaxBotix first test . . . . .	50
4.5	MaxBotix first test . . . . .	51
4.6	Maxbotix pulley test . . . . .	51
4.7	Maxbotix pulley test log . . . . .	52
4.8	JSN-SR04T . . . . .	52
4.9	JSN-SR04T Timing . . . . .	53
4.10	JSN-SR04T sensor log . . . . .	53

# List of Tables

2.1 Comparison of different deployment modes highlights the efficiency of UAV deployment. . . . .	25
---	----

# Chapter 1

## Introduction

### 1.1 Autonomous unmanned vehicles

Since the industrial revolution, autonomous machines have become a significant contributor to increased human productivity. From the steam engine and assembly line conveyor belt, autonomous machines take over repetitive, labor-intensive tasks and leave human with jobs requiring more attention to details but less physical energy. Every year, the list of tasks automated by machines grow bigger. Vehicles were one of the first few machines predicted to be automated, yet Autonomous Unmanned Vehicles (AUV) just recently became commercially available, although in smaller scales.

With the advent of commercially available small AUV, we can automate tasks such as surveying, sensor network distribution, and inspection, which previously require intensive human labor. Surveying with visual, sonar and laser sensor with Unmanned Aerial Vehicles (UAV) have become commercially available. UAV photography is growing into a booming business, with turn key solution packages. Enabling photo and movie studios to get aerial footage and pictures without the need for expensive helicopter rentals. UAV surveying with traditional or modified surveying equipment reduces the cost of surveying sites for constructions or archeological digs.

### 1.2 Deploying seismic microphones with AUV

Seismic microphones are used in seismic surveying to find subsurface deposits of natural resources. Seismic surveying can also be used to identify where earthquakes can happen. Traditionally, seismic microphones are connected 2 m or 3 m apart on a long



Figure 1.1: The heterogeneous sensor system presented in chapter 2: wireless Seismic-Darts and a SeismicSpider, both designed for UAV deployment.

cable. The cable is composed of 20 to 30 microphones and connected to one computer responsible for recording the reflected sound wave. Several cables can be laid out to cover the entire survey area, so the length of cable required is proportional to survey area. Transporting the cables means increased weight, and they can be difficult to maneuver and deploy on rough terrain. Surveyors will need to expend a lot of manual labor to distribute these sensors

Recently, nodal sensors with their own recording unit can be used, eliminated the need for cabling. However, these nodal sensors are still planted and recovered by hand, requiring surveyors to traverse rough terrain multiple times.

Our first use of AUV is to make nodal seismic microphone deployable from an Unmanned Aerial Vehicle (UAV). Our system can be seen in Fig. 1.1. The SeismicDart is a dart shaped, wireless capable sensor that can be dropped from a UAV to plant into the ground firmly. The SeismicSpider is a mobile six-legged robot rover with three seismic microphones for legs. The Spider can be deployed in a clearing where UAVs can access, then walk into a more covered area where it's hard for UAV to fly over and drop SeismicDarts. The system can be utilized to quickly deploy sensor asset for geoscience research [1] such as earthquake [2], and volcano [3] monitoring, defense operations [4], and wildlife monitoring [5, 6].

### **1.3 Destructive surveying of mosquito with UAV**

Mosquito-borne diseases kill millions of humans each year [7]. Because of this threat, governments worldwide track mosquito populations. Following individual mosquitoes is difficult because of their small size, wide-ranging flight, and preference for low-light. Tracking studies of individual mosquitoes have chosen to use small (1.2 m  $\times$  2.4 m) indoor regions [8], or mating swarms backlit against a solid background [9].

The dominant tools for tracking mosquito populations are stationary traps that are

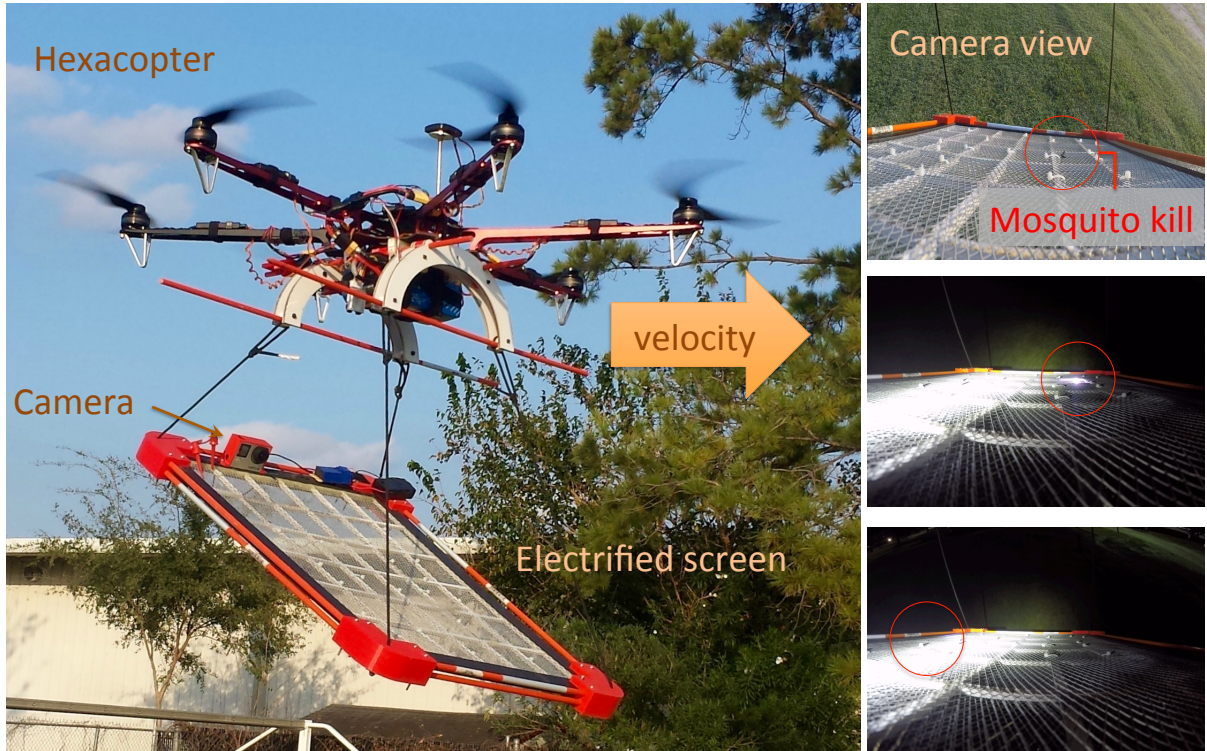


Figure 1.2: A hexacopter UAV carrying a 48 cm  $\times$  61 cm rectangular bug-zapping screen.

checked at weekly intervals (*e.g.*, Encephalitis Vector Surveillance traps and/or gravid traps [10]). Recent research has focused on making these traps smaller, cheaper, and capable of providing real-time data [11, 12]; however, they still rely on attracting mosquitoes to the trap. We present an alternate solution using an electrified bug-zapping screen mounted on an unmanned aerial vehicle (UAV) as shown in Fig. 1.2 to seek out the mosquitoes in their habitat. An onboard microcontroller monitors the voltage across the screen and records the time, GPS location, humidity, and altitude for each mosquito strike. At right are three frames recorded by the onboard camera showing mosquito hits, during the day (top) and at twilight. See attachment for videos of flight experiments [13]. As the UAV follows a path, it sweeps out a volume of air, temporarily removing all the mosquitoes in this volume. By monitoring the voltage across this screen, we can track individual mosquito contacts. UAVs have strict energy budgets, so optimized flight patterns are of crucial importance. As a consequence, putting the UAV to good use requires methods for computing trajectories that minimize energy consumption along the way,

but maximize the total volume of mosquitoes at visited locations.

## 1.4 Surveying underwater with drifting sensors

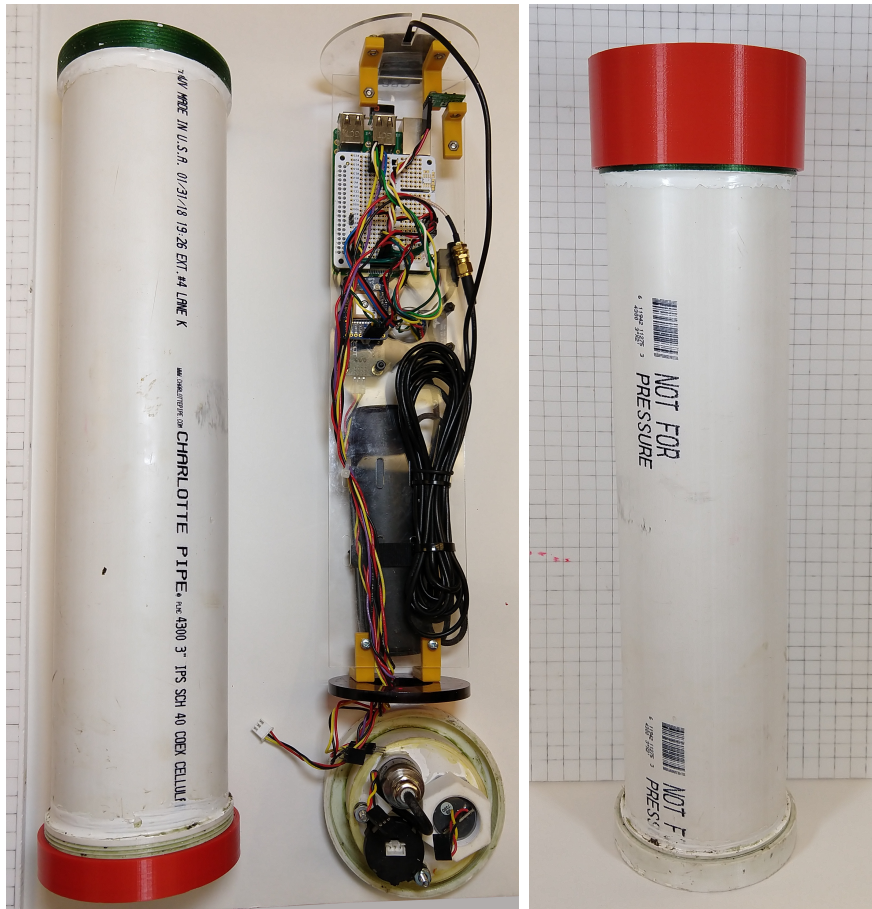


Figure 1.3: (Left) driftnode before assembly, the electronics are attached to a center acrylic plate. (Right) an assembled driftnode.

Humans know less about the ocean than they do about space. Because EM waves attenuate quickly in water, it is challenging to deploy wireless sensor network in water for permanent surveying post. A boat and crew need to be dispatched to survey a water surface. The crew can then manually deploy sensor at each location within the area for scientific research. The team will need to be dispatched periodically to monitor an area for border security or fishing enforcement. One crew cannot watch several areas simultaneously, so the man-hour required grows proportionally with area monitored.

This requires the need for several crews, or risk security incidence when an area is not monitored.

A wireless sensor network, composed of drifting sensors, deployed temporarily or permanently, can monitor an area for much longer with less labor needed. A UAV can be used to periodically visit these sensors, collecting their sensor logs and charging them. We present a drifting sensor platform, initially created by the University of South Carolina [14], as seen in Fig. 1.3. The drifting sensor is composed of a suite of underwater sensor: An underwater depth sensor, a pressure sensor, a turbidity sensor, 9-axis IMU and GPS location sensor. Our drifting sensor can broadcast its own wireless access point, which enables an AUV to collect data from the sensor at close range.

## Chapter 2

### UAV deployment of seismic microphones

This chapter describes research performed for the 2016 IEEE RA-L paper "A heterogeneous robotics team for large-scale seismic sensing", by S.K.V. Sudarshan, V. Montano, A. Nguyen, M. McClimans, L. Chang, R.R. Stewart, and A.T. Becker. [15]

I constructed the UAV, its landing gear and helped design the SeismicDart deployment unit. I piloted all UAV test and programmed the autonomous SeismicDart deployment flights. As pilot, I tested the positional repeatability of the SeismicDart drops and recorded the video footage used for the paper. I also helped construct, test and record results for the pneumatic cannon alternative method.

#### 2.1 Overview and related work

This chapter presents a *heterogeneous seismic sensing system*, composed of stand alone geophone nodes deployed from unmanned aerial vehicles UAV and autonomous rovers with geophone attached. We examine experimental data on geophone and soil coupling as a function of drop height and soil type. We then provide a software tool for analyzing and planning a survey mission's logistic. Our *heterogeneous sensor system* approach is designed to quickly and efficiently perform a survey with minimal manual labor for deployment and collection.

Sudarshan et al. [16] demonstrated a UAV equipped with four geophone sensors as landing gear. The UAV in [16] can fly to a pre-programmed waypoint and land, attaching the geophones to the soil.

The geophones in [16] had four problems: (1) a UAV was required for each addi-

tional sensor, (2) the force for planting the geophone was limited by the weight of the UAV, (3) the platform required a level landing site, (4) the magnets in the geophones distort compass readings, causing landing inaccuracy when autonomous.

The *SeismicDart* presented in this system eliminates the need for a separate UAV per sensor node. Dropping the SeismicDarts from height also allows for greater penetration, firmer coupling and does not need a level landing site. The new deployment unit also increase the distance between the SeismicDart's magnet and the UAV's magnetometer unit.

The SeismicSpider, our autonomous rover, can travel to survey locations inaccessible to UAV such as forests, thin atmosphere environments, caves or hard and rocky grounds which SeismicDarts cannot penetrate. The SeismicSpider can also be deployed by a UAV, as close to the survey node as possible, then move to the desired location.

### 2.1.1 Overview of seismic sensing theory

During seismic surveys, a source generates seismic waves that propagate under the earth's surface. These waves are sensed by geophone sensors and recorded for later analysis to detect the presence of resources. Fig. 2.1 illustrates the components of current sensors.

#### Geophones

Magnet-coil geophones contain a permanent magnet on a spring inside a coil. Voltage across the coil is proportional to velocity. Beneath the coil housing is a metal spike. Geophones are *planted* by pushing this metal spike into the ground, which improves coupling with the ground to increase sensitivity. The magnet-coil must be vertical. Misalignment reduces the signal proportional to the cosine of the error.

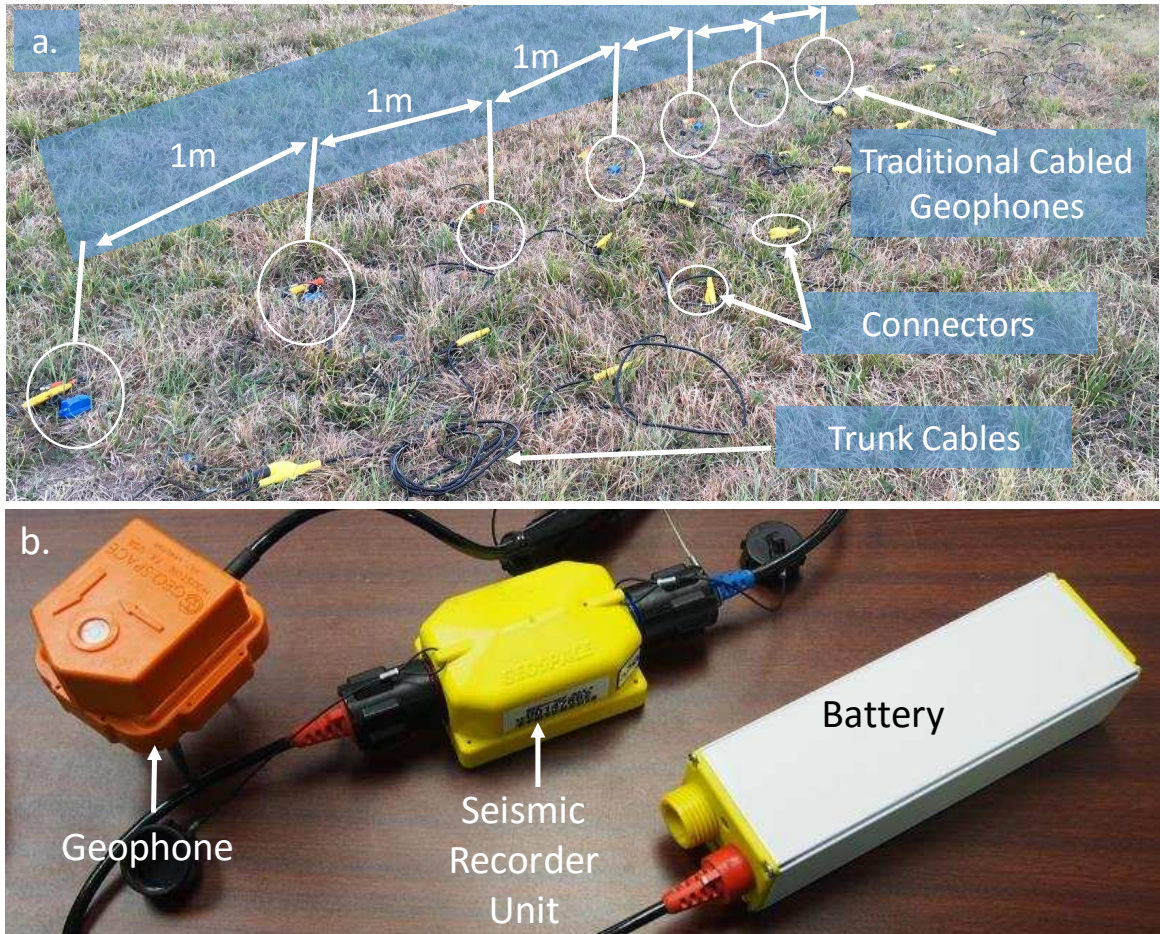


Figure 2.1: Comparing state-of-the-art seismic survey sensors. a) A traditional cabled system connects geophones. b) Autonomous nodal systems.

### Cabled systems

Hydrocarbon exploration extensively uses traditional *cabled systems* for seismic data acquisition. Geophones are connected to each other in series using long cables. This cable is then connected to a seismic recorder and battery. The seismic recorder consists of a micro-controller which synchronizes the data acquired with a GPS signal and stores the data onboard. This method of data acquisition requires many manual laborers and a substantial expenditure for transporting the cables. Rugged terrain makes carrying and placing cables labor intensive, and the local manual labor pool may be unskilled or expensive.

## Autonomous nodal systems

*Autonomous nodal systems* [17] are now being used to conduct seismic surveys. Unlike traditional cabled systems, autonomous nodal systems are not connected using cables. The sensor, seismic recorder, and battery are all combined into a single package called a *node* that can autonomously record data as shown in Fig. 2.1. Even in these systems the data is generally stored in the onboard memory and can only be acquired after completing the survey. This delay means errors cannot be detected and rectified while conducting the survey. Wireless autonomous nodes are a recent development. These systems can transmit data wirelessly in real time [18]. However, these systems still require manual laborers for planting the autonomous nodes at specific locations and deploying the large antennas necessary for wireless communication.

### 2.1.2 Related work

Seismic surveying is a large industry. The concept of using robots to place seismic sensors dates to the 1980s, when mobile robots placed seismic sensors on the moon [19]. [20] and [21] proposed using a mobile robot for terrestrial geophone placement. Plans are underway for a swarm of seismic sensors for Mars exploration [22]. Additionally, [23] and [24] proposed marine robots for hydrophone deployment underwater. Other work focuses on data collection, using a UAV to wirelessly collect data from multiple sensors [25]. Autonomous sensor deployment and mobile wireless sensor networks were studied in [26, 27, 28]. Heterogeneous mobile robotic teams were used for mapping and tracking in [29].

## 2.2 SeismicDarts

A SeismicDart combines a geophone (GS-100) with the fins and body of a lawn Jart™, using a 3D-printed chamber that encloses a WiFi-enabled microcontroller (par-

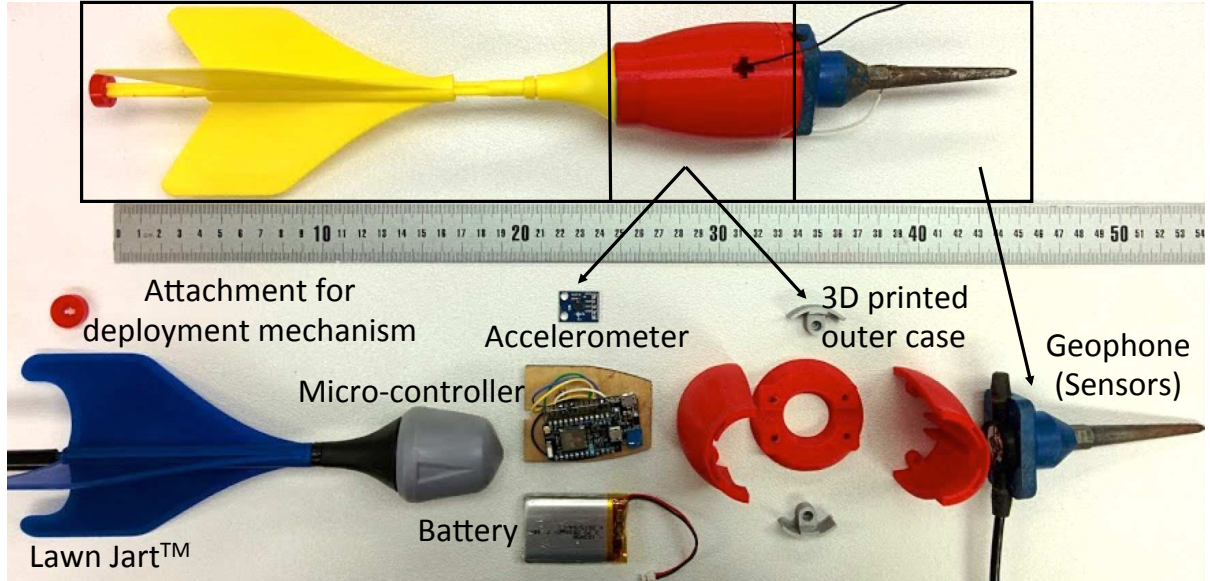


Figure 2.2: Components of the SeismicDart sensor: a lawn Dart™ fin, particle.io Photon™ micro-controller, 3D printed protective casing, and a geophone.

particle.io Photon™) as shown in Fig. 2.2. The center of the chamber is slotted to fit a wooden plate holding an accelerometer that transmits data wirelessly through the microcontroller. The centered accelerometer card allows placing the microcontroller and battery on opposite sides, balancing the dart. Designs and instructions to build a SeismicDart are available at [30].

### 2.2.1 Experiments

The following sections compare SeismicDart performance.

#### Drop Tests In Different Soils

Proper planting of a geophone requires good contact with the soil and the geophone to be in a vertical position. Geophone protocol classifies a geophone as well planted if the angle of deviation is less than  $10^\circ$  and the spike has at least 40 mm of penetration.

To determine how SeismicDarts perform in different soils, this experiment measured penetration depth and angle of deviation in seven different soil types as a function of drop

height. The soil types were categorized by compression strength, in  $\text{kg}/\text{cm}^2$ , measured using a soil pocket penetrometer (CertifiedMTP). Measurements for compression strength vary with a small deviation in measurement location, so we repeated this measurement 10 times at 10 different locations in each soil type and computed the average.

Experiments were conducted using the UAV to autonomously drop a payload of four SeismicDarts at the desired drop height. Tests were conducted at drop heights of 10, 15, 20, and 25 m. We measured the angle of deviation and penetration depth for each drop. The angular deviation was measured using two protractors. We measured penetration depth by marking where the spike met the soil, pulling the dart from the soil, and measuring the distance from the spike tip to the marking with calipers. We repeated this measurement 12 times for each soil type at each drop height. The soil compression strengths in these experiments ranged from  $0.056 \text{ kg}/\text{cm}^2$  for river sand, to  $4 \text{ kg}/\text{cm}^2$  for a hard-packed soccer field.

Because the four soil types with the lowest soil compression strength could be well-planted with low drop heights, we performed these tests manually. We filled 19 liter (5 gal.) buckets with four soil types and dropped the SeismicDart from six heights.

Experiment results plotting penetration depth as a function of drop height are displayed in Fig. 2.3, and angle of deviation as a function of drop height in Fig. 2.4. Both graphs are annotated with values for soil compression strength.

If a SeismicDart is dropped from a sufficient height into penetrable soil, the spike will be buried into the soil and the geophone will have a small angular deviation from vertical. Soils with higher compression strength require higher drop heights. Error bars show that variance decreases with drop height for angle of deviation and penetration depth. All drops from heights 20 m or more achieved the goals of an angle of deviation less than  $10^\circ$  and at least 40 mm of penetration.

The autonomous tests were conducted with 16 km/hr winds, demonstrating that

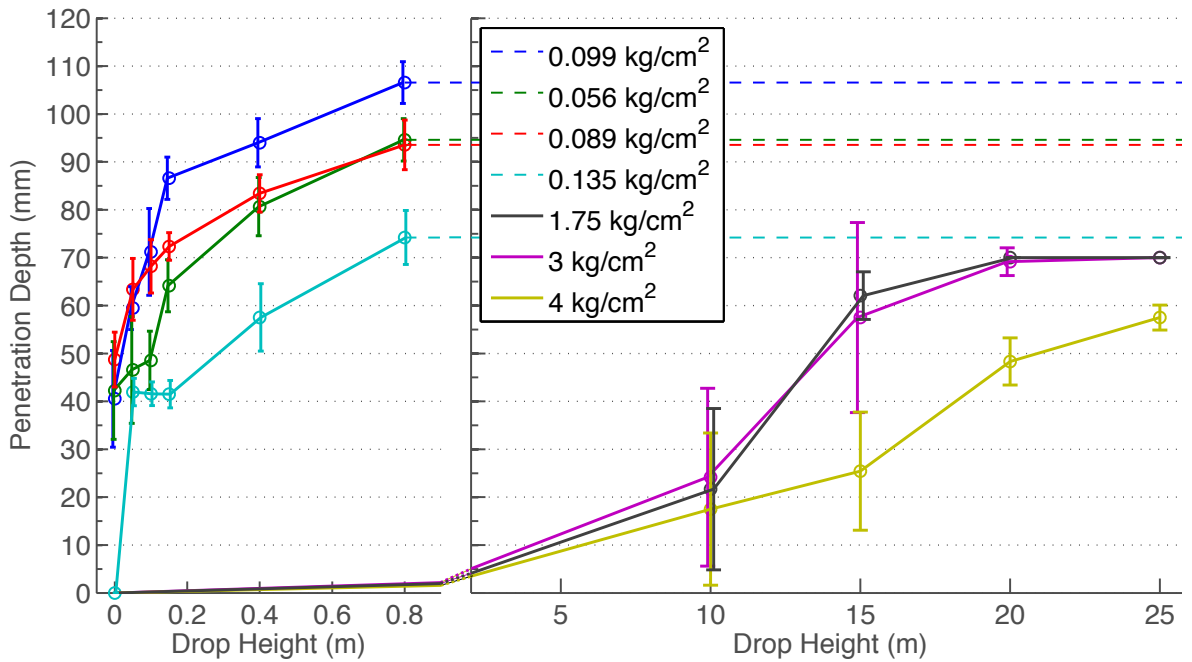


Figure 2.3: Drop height vs. penetration depth in seven soil types. Drops were performed autonomously and each data point represents 12 trials. Increasing the drop height increased the penetration depth for all seven soil types.

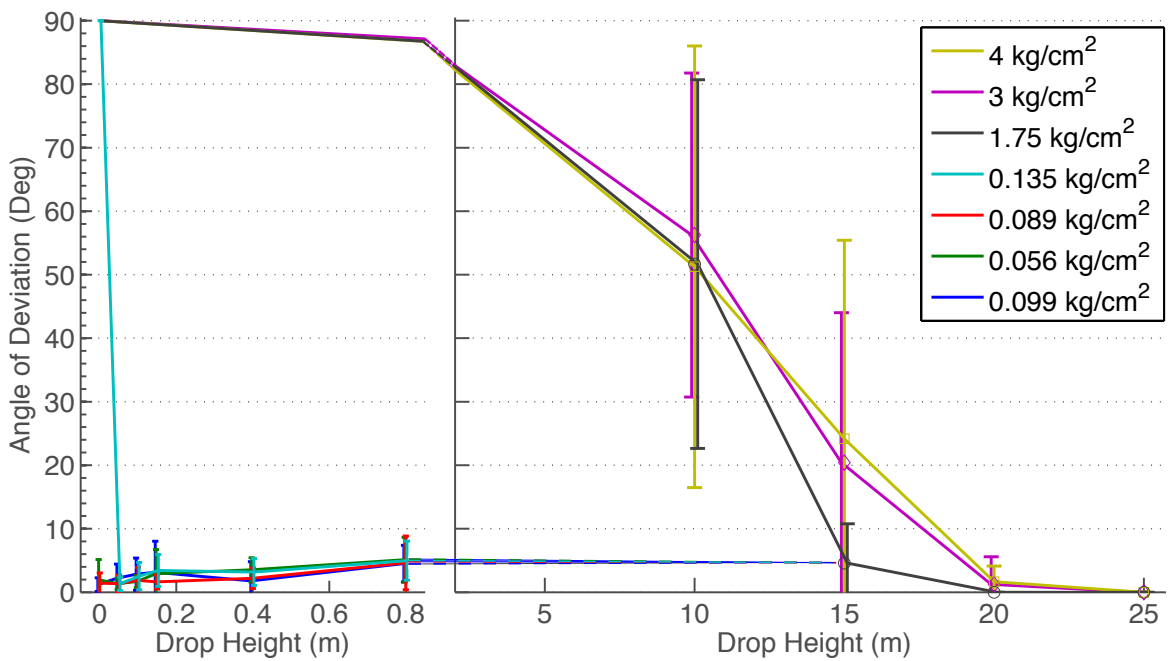


Figure 2.4: Drop height vs. angle of deviation in seven soil types. Drops were performed autonomously and each data point represents 12 trials. Increasing the drop height reduced the angle of deviation for all seven soil types.

drop heights 20 m or higher were sufficient to counter disturbances from the wind.

### Shot gather comparison

Geophysical explorationists often use thousands of geophones to conduct a seismic survey. As a proof-of-concept, this experiment ran a small-scale seismic survey to compare the performance of a traditional cabled four geophone system with readings from four autonomously deployed SeismicDarts. Flying autonomously at a drop height of 25 m, the UAV flew to GPS waypoints spaced 4 m apart and deployed one dart at each location. A seismic survey technician manually planted four traditional cabled geophones, each 10 cm from a deployed SeismicDart. A seismic wave was generated using a sledgehammer hitting a steel plate.

Results of the field test comparison between the traditional cabled geophone system and the SeismicDarts are shown in Fig. 2.5. Data were obtained using a *StrataVisor*, a device that can obtain, store, and plot the sensed data. The *StrataVisor* is extensively used with traditional geophone setups because the geophones can only sense vibrational waves and are dependent on other devices for storage and data processing. To allow a fair comparison with geophones, the SeismicDart’s ability to store sensed data was not used in this experiment. The *StrataVisor* records the geophone voltage at 2000 Hz, using a 24 bit ADC.

The readings from both systems are qualitatively similar, with no discernible phase or amplitude differences. Let  $X$  be measurements from the traditional geophone and  $Y$  the corresponding voltages from a SeismicDart. The percent peak-to-peak error and normalized root-mean-square error (NRMSE) are defined as

$$e_{pp} = 100 \left( \frac{\max(X) - \min(X)}{\max(Y) - \min(Y)} - 1 \right) \text{ and} \quad (2.1)$$

$$\text{NRMSE} = \frac{100}{\max(X) - \min(X)} \sqrt{\frac{\sum_{i=1}^n (X_i - Y_i)^2}{n}}. \quad (2.2)$$

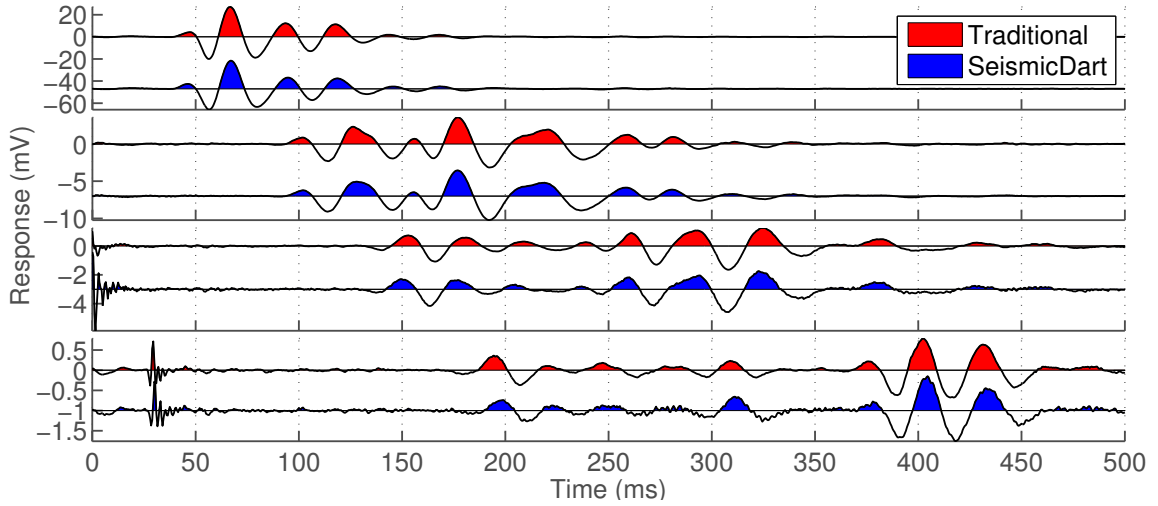


Figure 2.5: Raw voltage data from shot gather comparison of four traditional geophones and four autonomously dropped SeismicDart sensors.

The peak-to-peak errors were  $[-6.33, -1.15, -1.81, 9.84]$  % for sensors at  $[4, 8, 12, 16]$  m from the source. The NRMSE were  $[1.05, 1.27, 3.98, 4.39]$  % for sensors at  $[4, 8, 12, 16]$  m from the source. Readings were also compared using a Pearson product-moment correlation coefficient, which gives a correlation measurement between  $-1$  and  $+1$  where  $+1$  is total positive linear correlation:

$$\rho_{X,Y} = \frac{E[(X - \mu_X)(Y - \mu_Y)]}{\sigma_X \sigma_Y}. \quad (2.3)$$

The correlation coefficients were  $\rho_{4\text{ m}} = 0.9813$ ,  $\rho_{8\text{ m}} = 0.9836$ ,  $\rho_{12\text{ m}} = 0.8600$ ,  $\rho_{16\text{ m}} = 0.8114$ . These correlations decrease with distance. The SeismicDart is subject to low-amplitude noise, which is easiest to see in the fourth sensor because it was 16 m from the seismic source and thus had the lowest signal amplitude. This noise is potentially due to wind striking the SeismicDart's fin. The effect of noise can be mitigated by using larger seismic sources such as a vibration truck or explosives.

### 2.2.2 SeismicDart deployment and retrieval

First, the SeismicDarts are loaded onto to a UAV. Currently, a maximum of four sensors can be dropped in a single flight. The flight plan communicated to the UAV



Figure 2.6: SeismicDart retrieval and redeployment. See video attachment.

provides a GPS waypoint for each SeismicDart. The UAV flies to and drops a SeismicDart at each waypoint, then returns home.

Deployment is only one part of a survey. Large surveys require moving and reusing sensors. Because SeismicDarts are more expensive than standard geophones, rapid reuse is essential. The UAV has an underslung hook for picking up a SeismicDart. Retrieval is facilitated by attaching a wire loop to the SeismicDart tail. This loop provides a target 300 mm in diameter for the hook, yet still allows autonomous deployment, as shown in Fig. 2.6. Currently, retrieval is performed by manually piloting the UAV, but the loop size is within the accuracy of a UAV equipped with RTK GPS.

### 2.3 SeismicSpider

The SeismicSpider, shown in Fig. 2.7, is built from the Six Hexapod kit designed by EZ-Robots. Each of the six legs is powered by two 15 kg cm lever servos. Three legs were replaced by three GS-20DM 14 Hz geophones from Geospace Technologies. The remaining three legs were designed to match the geophone dimensions.

Our initial plan to use three geophones required the spider to raise the three inactive legs while acquiring data. This lack of support caused excessive strain on the three servo motors responsible for holding the spider upright, introducing unwanted vibration into the system. Positioning the geophone legs at  $20^\circ$  to normal enhances stability and relieves the excessive stress on the servos. The three geophones were in series, so with

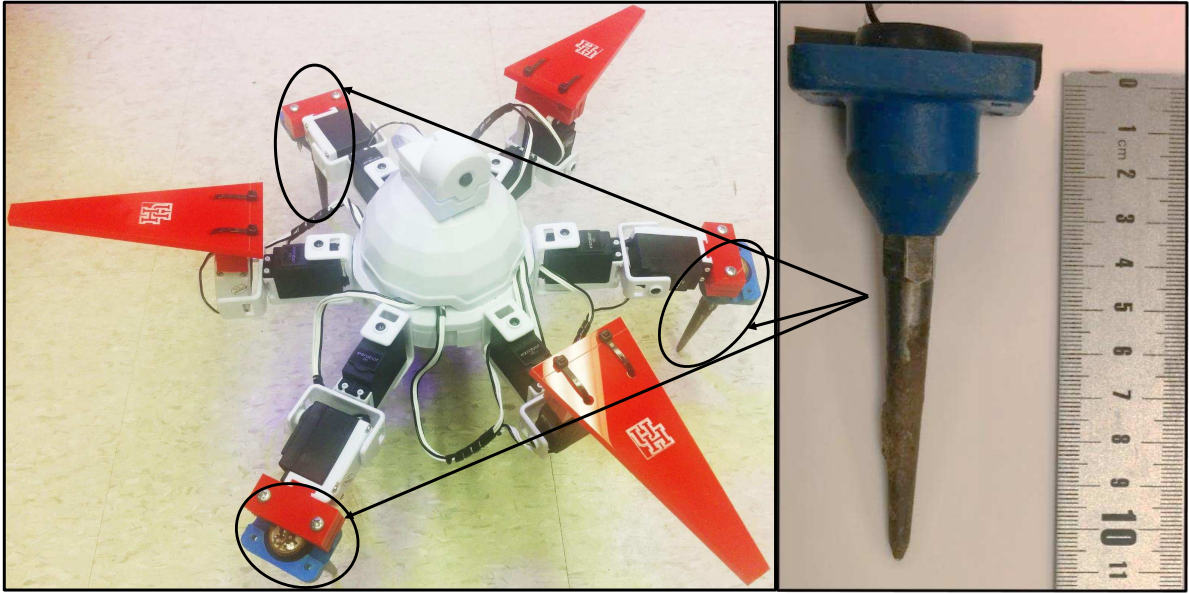


Figure 2.7: The SeismicSpider is a six-legged mobile robot where geophones replace three legs. It is drone deployable, can sense and record seismic data, and can move to desired locations, including terrain the SeismicDart cannot access.

each geophone leg angled inward, superposition replicates the signal from one vertical geophone.

Traditional geophones are mounted in an insulated, shock-resistive enclosure on a spike. The spikes, varying in length, are inserted into the ground to ensure a firm coupling with the environment. The design of our SeismicSpider prevents full depth insertion of the 88 mm spikes.

To overcome the coupling issue we are using three geophones per station compared to the typical one. Our immediate goals were to compare amplitude response to that of a standard single station.

### 2.3.1 Shot gather comparison

A line of twenty-four geophones (GS-20DM 14 Hz) were laid out at one-meter intervals with our inline source seven meters from the nearest geophone. Beginning from the farthest offset of 31 m we manually aligned the Spider with the corresponding

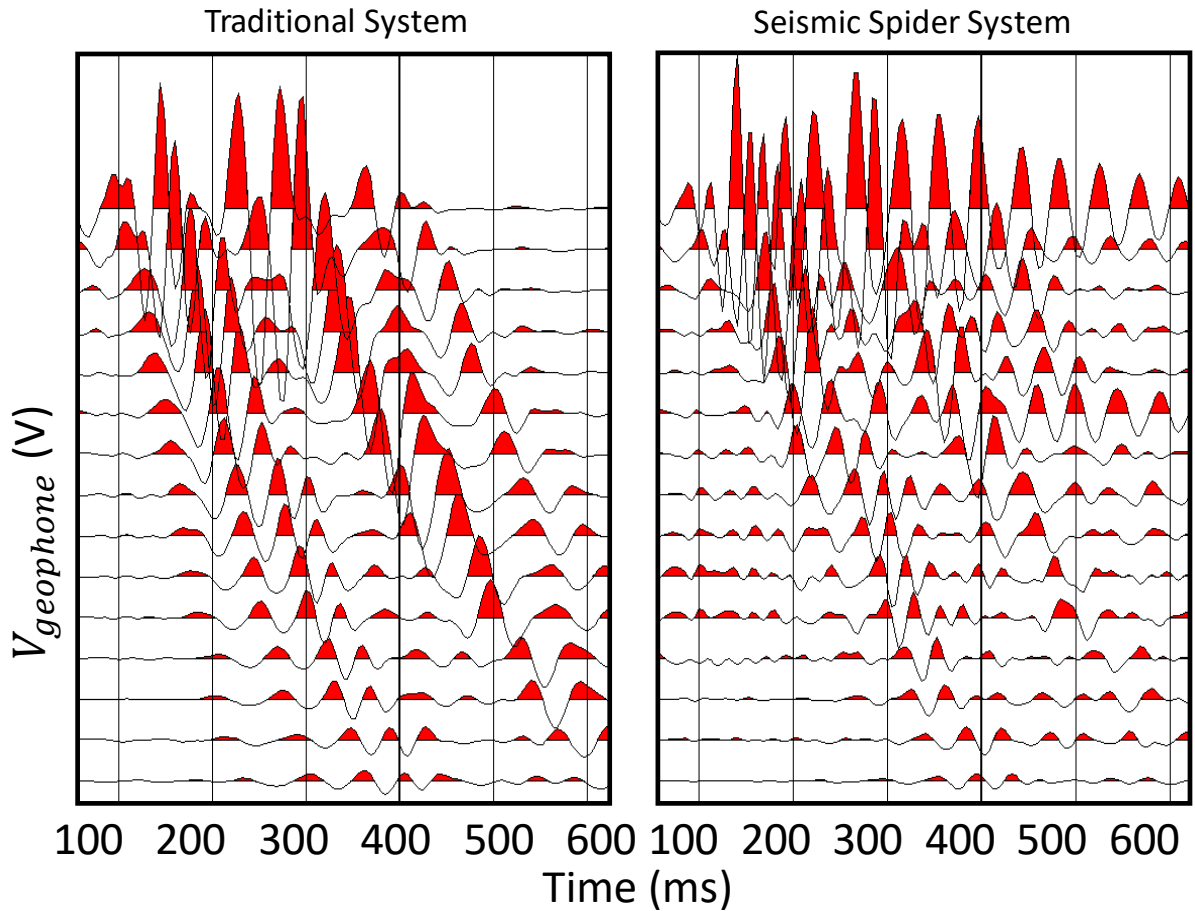


Figure 2.8: Shot gather comparison of traditional geophones vs. SeismicSpider.

geophone, fired the source, then moved one meter ahead.

Data from the shot gather comparison is shown in Fig. 2.8. The response for three geophones in series was 5 dB greater than a single geophone. The geophone wires proved insufficient to insulate against 60 Hz noise. Hence the raw data from the traditional setup as well as the SeismicSpider was processed with a (3-50) band-pass filter. Finally, the SeismicSpider data was attenuated by  $-5\text{dB}$  to level the comparison.

### 2.3.2 Deploying and retrieving the SeismicSpider

The UAV's purpose is to deploy sensors at desired GPS waypoint locations. The SeismicSpider is a mobile robot, but it is substantially slower than the UAV. The UAV carrying the SeismicSpider flew autonomously to a programmed waypoint. The deploy-

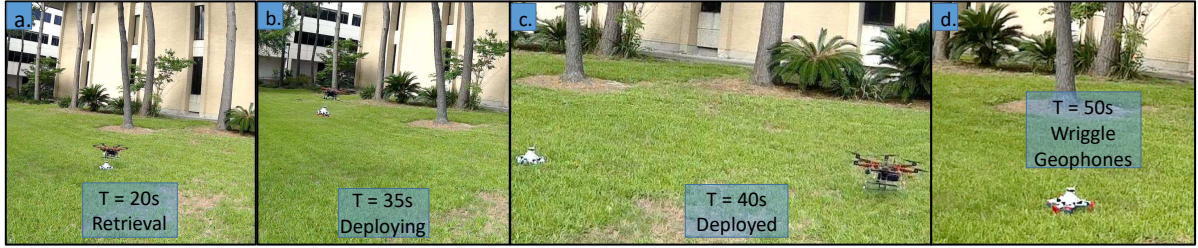


Figure 2.9: SeismicSpider retrieval and redeployment. See video attachment.

ment mechanism included a hook controlled by a servo attached to the UAV. The UAV lowered to a waypoint 0.5 m from the ground, then the servo was triggered to unhook the SeismicSpider. The SeismicSpider was then wirelessly powered on. The SeismicSpider also has an onboard GPS, enabling it to navigate to desired waypoints. After walking to the sensing location, the SeismicSpider was programmed to shake its three non-sensing legs to plant its geophone legs into the ground. Currently, autonomous deployment of sensors is implemented, but the retrieval is piloted. Combining the mobility of the SeismicSpider with the speed of the UAV enables reaching locations inaccessible by air or impossible to penetrate by SeismicDarts. Fig. 2.9 shows the SeismicSpider being retrieved and then redeployed by a UAV.

## 2.4 UAV and deployment unit

The UAV is a custom-built, 1.77 m wingspan hexacopter, controlled by a Pixhawk flight controller running ArduPilot Mega flight software. The UAV has a 3DR GPS module using the UBlox NEO-7 chipset.

The deployment mechanism allows the UAV to carry four SeismicDarts in a circular array, and release them when it reaches the desired GPS location, one at a time. The rear of the dart has a circular tip that locks into the deployment mechanism, and rests on a rectangular slot-path. A servomotor rotates the dart tips through the rectangular slot-path, allowing darts to release from a circular opening, as shown in Fig. 2.10.

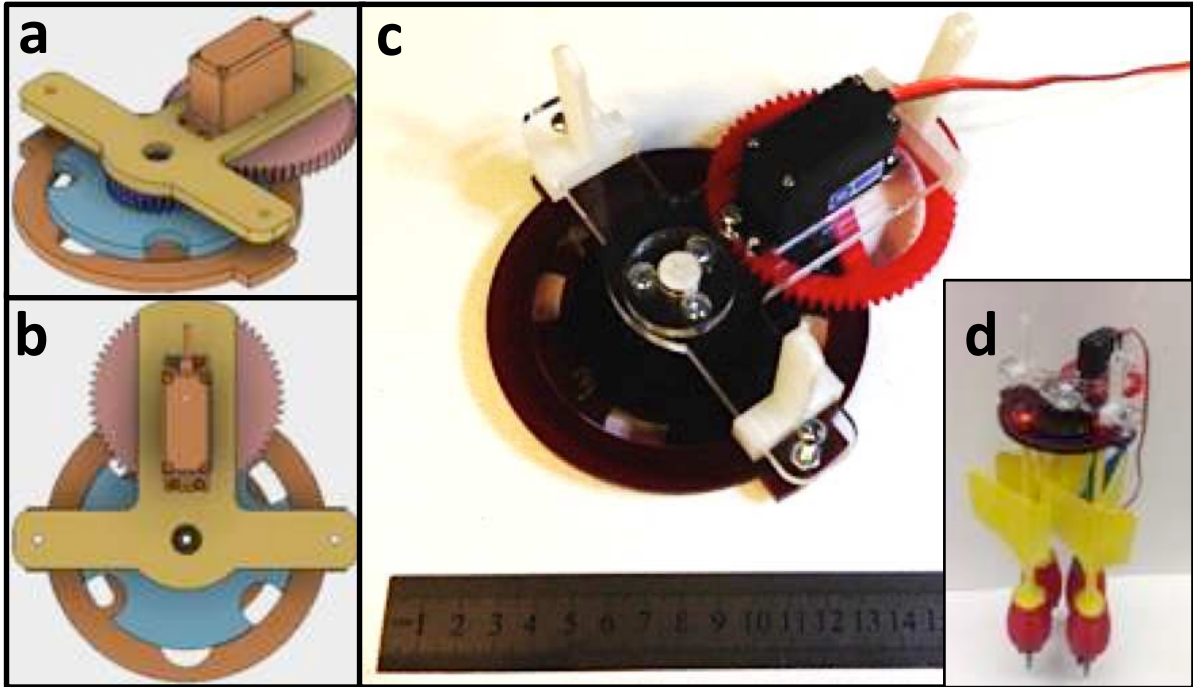


Figure 2.10: Deployment system for dropping SeismicDarts from the UAV. Pictured design holds four darts, but can be scaled according to the UAV's carrying capacity.

#### 2.4.1 Autonomous drop demonstration and accuracy

The current UAV can place a SeismicDart within  $\pm 1$  m of the desired location. This range is within tolerances for seismic surveys because often features (rocks, water, etc.) exist that require this amount of error from theoretically assigned locations and some survey designs include a random placement component to improve noise cancellation.

To accurately perform a seismic survey, the sensors do not need to be placed accurately, but their position must be known within  $\approx 0.01$  m. Knowledge of the exact location compensates for placement inaccuracy. Localization can be achieved by placing an RTK GPS in each dart. A lower-cost solution would use an RTK GPS on the SeismicDrone and perform image registration with the downward facing camera. As shown in the multimedia attachment, even at a 25 m drop height a planted dart occupies dozens of pixels, enabling cm-level localization accuracy.

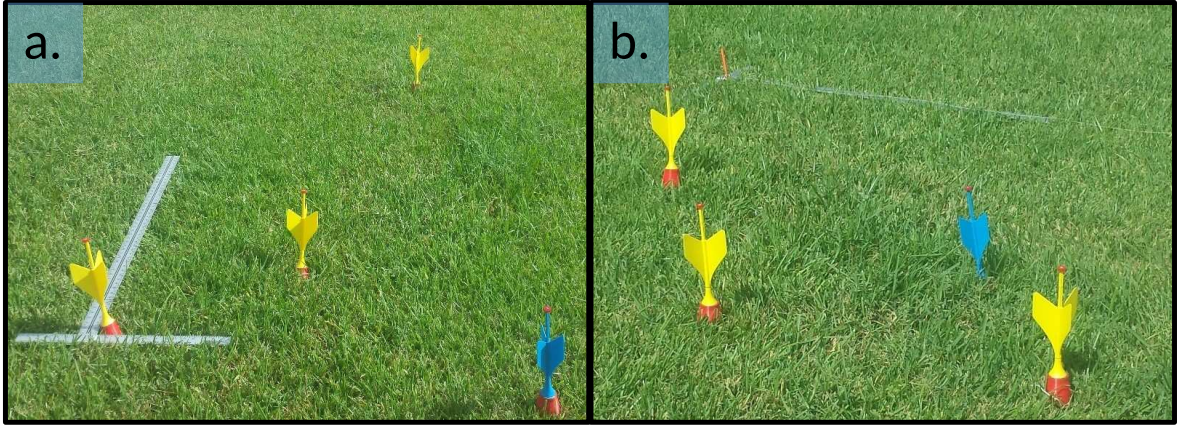


Figure 2.11: a) First set of darts with reference axes. b) Third dart set.

For the accuracy test, six sets of darts, four darts in each set, were dropped on the same GPS waypoint. Between each drop, the UAV traveled to a nearby GPS waypoint to cancel out the flight controller’s stable hover. The UAV then returned to the launch platform to be reloaded, we recorded the dart landing positions, collected the darts, and reloaded the darts on the UAV for the next deployment set. The measurement method of the darts’ positions are shown in Fig. 2.11. Results are shown in Fig. 2.12.

#### 2.4.2 Height vs. penetration depth

FAA rules require that UAVs fly below 400 feet (122 m). Our highest drop tests were from 25 m, and resulted in well-planted geophones on a compacted field with density 4 kg/cm<sup>2</sup>. Harder soils may require faster impact velocity, so this section examines possible impact velocities as a function of drop height. For ease of analysis, we will assume the SeismicDart has a constant coefficient of drag  $C_d$  and that the drag force is proportional to velocity squared and equal to  $\frac{1}{2}v^2\rho AC_d$ , where  $v$  is the velocity,  $A$  the cross-sectional area and  $\rho$  the density of air. The tests were performed near sea level, so  $\rho \approx 1.225 \text{ kg/m}^3$ . The dart body is 0.06 m in diameter so  $A = 0.028 \text{ m}^2$ . We will assume the dart  $C_d$  is between that of a streamlined body  $C_d = 0.04$  and that of an arrow

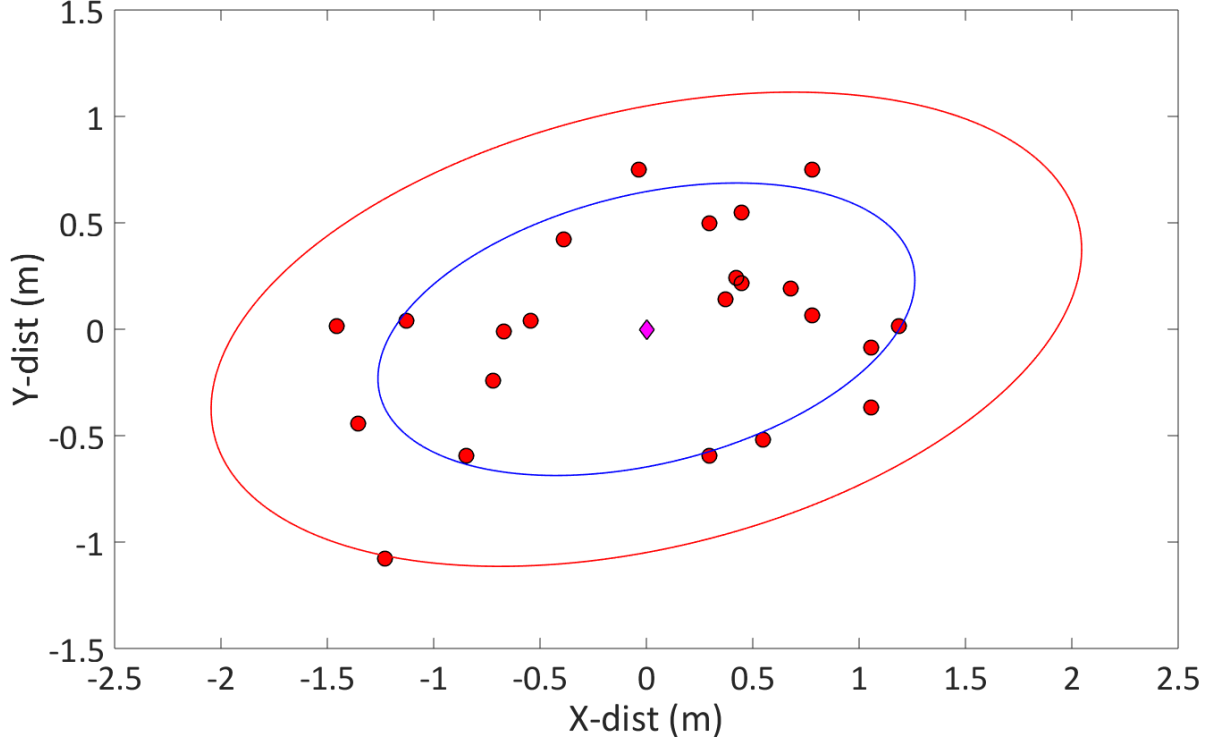


Figure 2.12: Targeting accuracy. Circles show landing locations of 24 darts, each commanded to drop at the same GPS location. The mean position is marked by a diamond, ellipses show  $\sigma$  and  $2\sigma$  covariance.

$C_d = 1.5$  [31], and choose that of a sphere  $C_d = 0.47$ . The terminal velocity is then

$$v_T = \sqrt{\frac{2mg}{\rho AC_d}} \approx 59 \text{ m/s}. \quad (2.4)$$

The velocity at impact is a function of the drop height  $h$ :

$$v_{\text{impact}} = v_T \sqrt{1 - e^{-\frac{\rho AC_d h}{m}}} \approx 59 \sqrt{1 - e^{-0.008h}} \text{ m/s}. \quad (2.5)$$

With  $C_d = 0.47$ , our drop from 25 m achieves only 43% the terminal velocity (21.1 m/s), and for  $C_d = 0.04$  only 13% terminal velocity (22.0 m/s). Dropping from the maximum FAA height of 122 m would generate an impact velocity of 39 m/s with  $C_d = 0.47$ , enabling penetration of harder soils.

### 2.4.3 Robustness

The darts are robust. One of the darts used for the shot gather in Fig. 2.5 was a veteran of 120 drops. The most damage observed occurred when we dropped a Seismic-

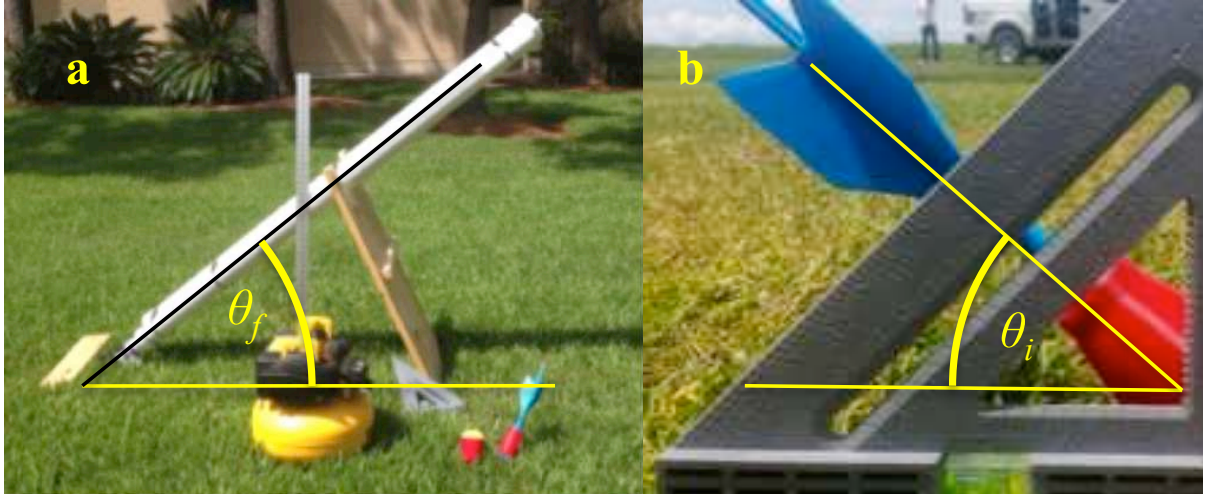


Figure 2.13: A pneumatic launcher for SeismicDarts. Ballistic dart deployment has limited usefulness because the incident angle is equal to the firing angle.

Dart 10 m onto a bed of rocks, each approximately 0.1 m in diameter. The steel spike of the dart was blunted, but this damage was quickly compensated by resharpening with a hand file and the SeismicDart was ready to redeploy.

## 2.5 Comparison

### 2.5.1 Ballistic deployment

To compare an alternative deployment mechanism we built the pneumatic cannon shown in Fig. 2.13a. The pneumatic cannon is U-shaped, 2 m in length, with a 0.1 m (4 inch) diameter pressure chamber and a 0.08 m (3 inch) diameter firing barrel, connected by an electronic valve (Rain Bird JTV/ASF 100). The cannon is aimed by selecting an appropriate firing angle  $\theta_f$ , azimuth angle, and chamber pressure. The reachable workspace is an annular ring whose radius  $r$  is a function of the firing angle and initial velocity  $v$ . Neglecting air resistance, this range is found by integration:

$$r = \frac{v^2}{g} \sin(2\theta_f). \quad (2.6)$$

Initial velocity is limited by the maximum pressure and size of the pressure chamber. The cannon used SCH 40 PVC, which is limited to a maximum pressure of 3 Mpa (450

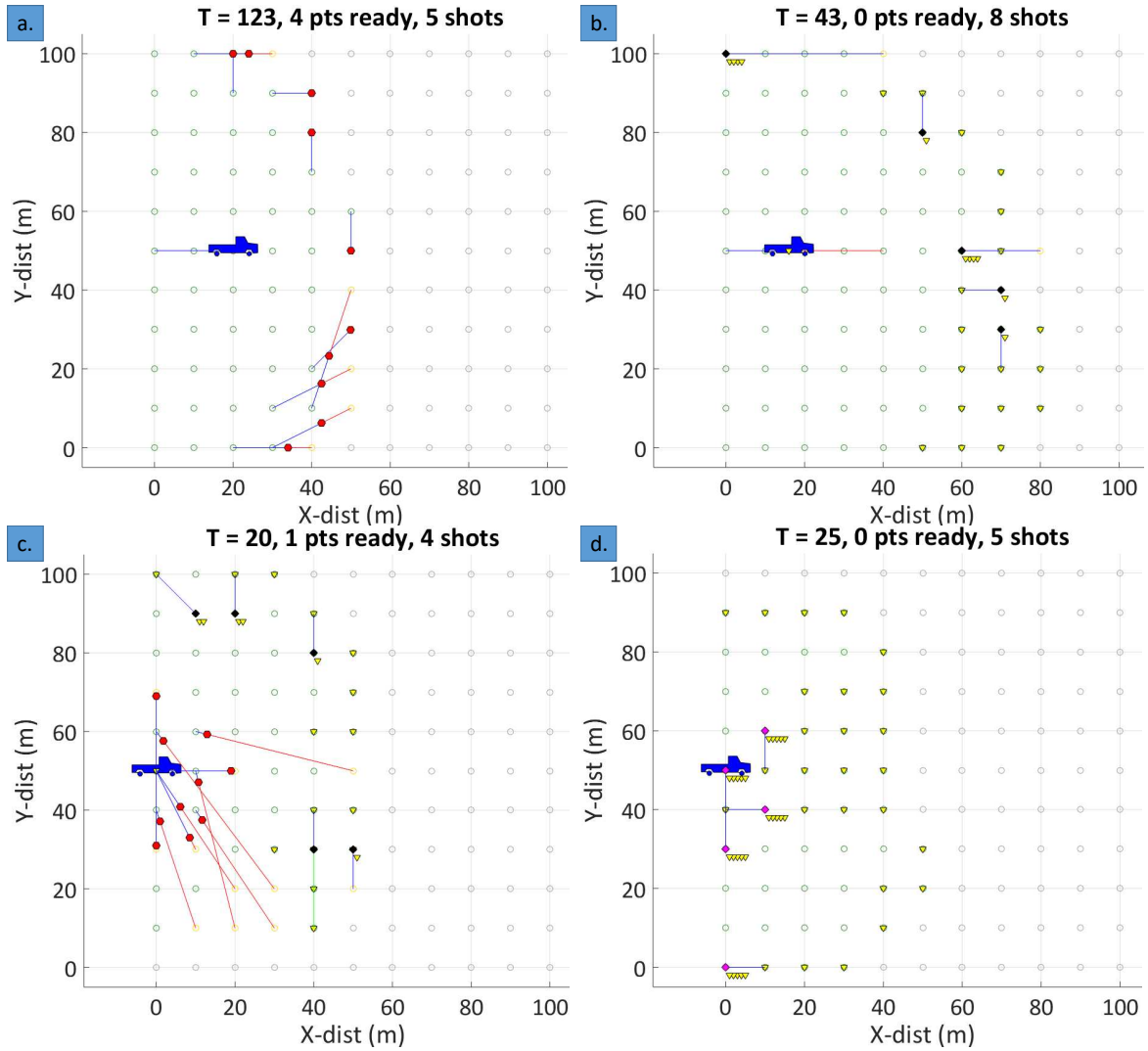


Figure 2.14: Screenshots of simulations to estimate time take by different team surveying 100 m  $\times$  100 m grid: a) only SeismicSpiders b) SeismicDarts and deployment system c) heterogeneous system d) human workers.

psi).

We charged our system to 1 Mpa (150 psi), and achieved a range of  $\approx 150$  m. This range is considerably smaller than the UAV's range, which when loaded can complete a round trip of  $\approx 1.5$  km.

A larger problem, illustrated in Fig. 2.13, is that angle of incidence  $\theta_i$  is equal to the firing angle  $\theta_f$ . Maximum range is achieved with  $\theta_f = 45^\circ$ , but this angle of incidence reduces the geophone sensitivity to  $\cos(\theta_f) \approx 0.7$ . The placement accuracy of the cannon

Table 2.1: Comparison of different deployment modes highlights the efficiency of UAV deployment.

Test	Type	Numbers of Units	Survey Time (s)	Velocity (m/s)
1.	SeismicSpiders	5000 SeismicSpiders	73,893	0.2
2.	UAVs, SeismicDarts	500 UAVs, 5000 SeismicDarts	1,216	20
3.	Workers	500 Workers, 5000 Sensors	7,371	1.38

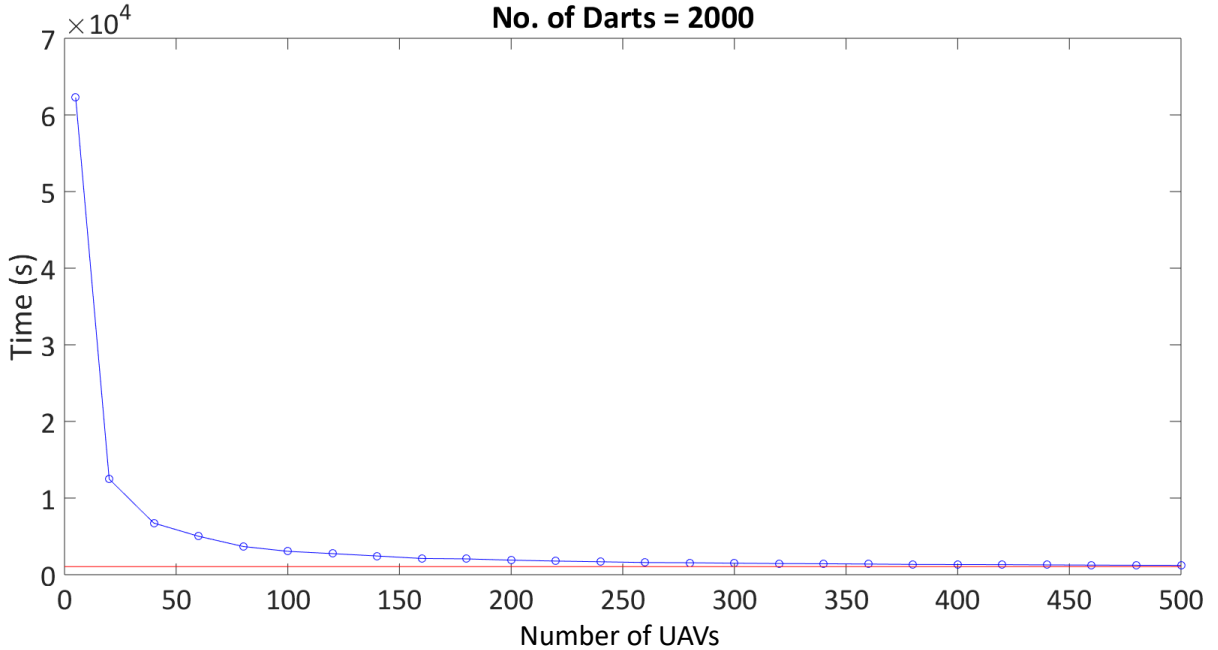


Figure 2.15: Survey time for a 1 km × 10 km region for different numbers of UAVs.

is lower than the UAV because a fired dart must fly over a longer distance than a dropped dart. Safety reasons also limit applications for a pneumatic launcher.

### 2.5.2 Simulation studies

A scheduling system to compare time and costs for seismic surveys with varying numbers of UAVs, SeismicSpiders, SeismicDarts, and human laborers was coded in MATLAB, available at [32]. In each simulation, a seismic source must be measured at every survey point. The scheduler must assign each sensor (SeismicDart or SeismicSpider) to an unmeasured survey point and assign each UAV or human worker a dart to pickup or

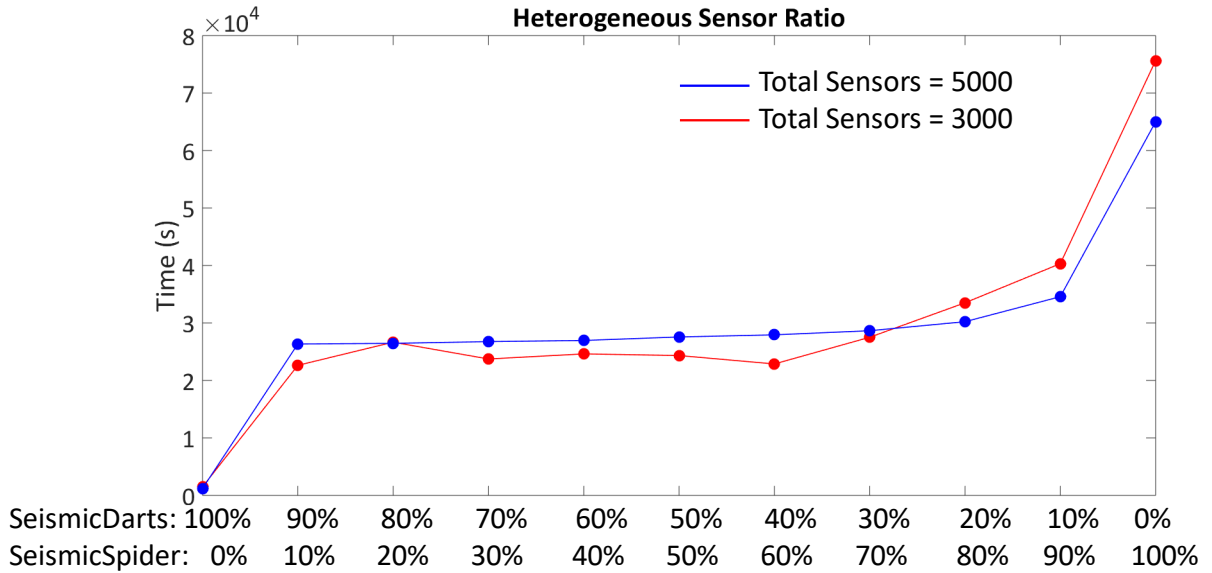


Figure 2.16: Survey time for different sensor ratios. The total number of sensors {5000, 3000} were kept constant. Ten darts were provided for each UAV.

deploy. Once a sensor reaches a survey point, that sensor must wait until a seismic source is measured. A vibration truck (blue) provides the seismic source. Motion planning uses a centralized, greedy strategy.

Frames from four different cases on a small survey region are shown in Fig. 2.14 on a  $100\text{ m} \times 100\text{ m}$  area with survey points at 10 m spacing: a.) simulates 10 SeismicSpiders; b.) simulates 5 SeismicUAVs deploying 50 SeismicDarts. Each UAV was allowed to carry up to 4 darts; c.) simulates 10 SeismicSpider, 5 SeismicUAVs and 50 SeismicDarts; d.) simulates 5 human workers deploying 75 SeismicDarts. Each worker was allowed to carry up to 10 darts. Survey points are grey circles if unmeasured and green if measured. The simulation uses red hexagons for SeismicSpiders, black diamonds for UAVs, inverted yellow triangles for SeismicDarts, and magenta diamonds for human workers. The assigned motion path for each sensor is colored magenta and the path completed is blue.

This tool allows us to examine engineering and logistic trade-offs quickly through simulations. For example, Fig. 2.15 assumes a fixed number of darts and examines the

finishing time with 5 to 500 UAVs. The time required decays asymptotically, but 140 UAVs requires only twice the amount of time required for 500 UAVs, indicating 140 UAVs are sufficient for the task. Substantial cost savings can be obtained by selecting the number of UAVs required to complete within a certain percentage greater than the optimal time.

The tool is useful for comparing the effectiveness of heterogeneous teams. Table 2.1 compares surveying a  $1 \text{ km} \times 10 \text{ km}$  strip of land with teams of (a) 5000 SeismicSpiders, (b) 500 UAVs and 5000 SeismicDarts, (c) 500 humans and 5000 geophones. Team (b) completed six times faster than team (c). In Fig. 2.16, the total number of mobile agents are constant, but the percentage of UAVs and SeismicSpiders are varied. 10 SeismicDarts were provided for each UAV. Increasing the percentage of UAVs lowers the deployment time because UAVs move 20 m/s but SeismicSpiders move 0.2 m/s. The velocity difference makes UAV deployment time-efficient.

## 2.6 Future work

This chapter presented a *heterogeneous sensor system* and technique for autonomous geophone deployment. The *heterogeneous sensor system* compose of two components, UAV deployable SeismicDarts, mobile SeismicSpider. The work in this chapter allow us to automate tasks that currently require a much more manual labors in hazardous environment.

The SeismicDart's output is comparable to well-planted geophones. For hard surfaces where the SeismicDart could not penetrate, we presented an autonomous alternative, the SeismicSpider. The SeismicSpider is mobile, can actively adjust its sensors to ensure ground contact and vertical placement, and can be deployed and retrieved by UAVs.

Autonomous deployment was conducted using GPS, proving human involvement

could be minimized by adopting the proposed technique. Hardware experiments compared the autonomous system to manual planting and ballistic deployment. Simulation studies show time and cost savings over traditional manual techniques.

Future systems should be weatherized and optimized for cost, robustness, range, and speed. Soil maps could be used to plan a survey, allocating SeismicSpiders to rocky or forested areas and SeismicDarts to penetrable soils. These maps can be made more accurate using drone-carried ground penetrating radar [33]. Alternatively, the Seismic-Dart's internal accelerometer also provides feedback on the quality of the plant. As shown in Fig. 2.4, angular deviations indicate a higher drop height is needed.

## Chapter 3

# Using a UAV for destructive surveys of mosquito population

This chapter presents research performed for the 2018 ICRA paper "Using a UAV for destructive surveys of mosquito population", by A. Nguyen, D. Krupke, M. Burbage, S. Bhatnagar, S.P. Fekete, and A.T. Becker. [34]

I constructed the UAV and the attachment of the net, as well as assisted in early generations of the net. I piloted all UAV test and programmed the autonomous tests of our algorithm and data collection. I also designed the method to measure powerconsumption of the UAV and analyzed the data.

### 3.1 Overview and related work

*Mosquito control solutions:* Mosquito control also has a long history of efforts associated both with monitoring mosquito populations [35] and with eliminating mosquitoes. The work involves both draining potential breeding grounds and killing living mosquitoes [36]. An array of insecticidal compounds has been used with different application methods, concentrations, and quantities, including both larvicides and compounds directed at adult mosquitoes [37].

Various traps have been designed to capture and/or kill mosquitoes with increasing sophistication in imitating human bait, as designers strive to achieve a trap that can rival the attraction of a live human [38]. In recent history, methods have also included genetically modifying mosquitoes so that they either cannot reproduce effectively or cannot transmit diseases successfully [39], and with the recent genomic mapping of mosquito

species, new ideas for more targeted work have been formulated [40].

Popular methods to control mosquitoes such as insecticides are effective, but they have the potential to introduce long-term environmental damage and mosquitoes have demonstrated the ability to become resistant to pesticides [41]. Traditional electrified screens (bug zappers) use UV light to attract pests but have a large bycatch of non-pest insects [42]. This chapter introduces techniques using bug zappers mounted on unmanned vehicles to autonomously seek out and eliminate mosquitoes in their breeding grounds and swarms. Instrumentation on the bug zappers logs the GPS location, altitude, weather details, and time of each mosquito hit. Mosquito control offices can use this information to analyze the insects' activities. The device can be mounted on a remote-controlled or autonomous unmanned vehicle. If autonomous, the vehicle can use the data collected from the electrified screen as feedback to improve the effectiveness of the motion plan.

*Robotic pest management:* As GPS technology has flourished and data processing has become cheaper and more readily available, researchers have explored options for implementing the new technologies in breeding ground removal [43] and more effective insecticide dispersion [44]. Low-cost UAVs for residential spraying are under development [45]. Even optical solutions have been considered, including laser containment [46] or, by extension, exclusion and laser tracking and extermination [47].

*Robotic coverage:* Robotic coverage has a long history. The basic problem is one of designing a path for a robot that ensures the robot visits within  $r$  distance of every point on the workspace. For an overview see [48]. This work has been extended to use multiple coverage robots in a variety of ways, including using simple behaviors for the robots [49, 50].

The classic *Travelling Salesman Problem (TSP)* is generalized to the *Lawnmower Problem* [51], which try to cover the most area with a tool of a nontrivial size. For minimizing the turn cost of coverage path, Arkin et al. [52] showed that finding minimum

turn tours in grid graphs is NP-hard. The complexity of finding a set of multiple cycles that cover a given set of locations at minimum total turn cost had remained elusive for many years; *Problem 53* in *The Open Problems Project* asks for the complexity of finding a minimum-cost (full) cycle cover in a 2-dimensional grid graph. Arkin et al. showed [52] that the full coverage variant in *thin* grid graphs (which do not contain a  $2 \times 2$  square, so every pixel is a boundary pixel) is solvable in polynomial time.

## 3.2 Hardware design

This section examines the components of the mosquito UAV system, shown in Fig. 1.2. This includes the UAV, electrified screen, surveying electronics, and a discussion of the energy budget.

### 3.2.1 The UAV

The UAV is a custom-built, 177 cm wingspan hexacopter, controlled by a Pixhawk flight controller running ArduPilot Mega flight software. The UAV has a 3DR GPS module using the UBlox NEO-7 chipset.

### 3.2.2 Screen design

The mosquito screen is designed to eliminate high density mosquito populations. This screen was constructed from two expanded aluminum mesh panels, spaced apart by 3 mm thick ABS grid. These mesh panels have 12 mm diamond-shaped openings, and is held taught by nylon bolts around the perimeter. The bottom mesh panel is offset by half a diamond (6 mm) to the right to ensure all insects greater than 6 mm cannot pass through the net. The top mesh is held at the reference voltage and the bottom mesh is energized to 1.8 kV above the reference voltage.

The perimeter is reinforced by two sets of 7 mm diameter fiberglass rods that are

inset into 3D printed corner fixtures. These rods protect the frame from getting damaged from any side, and allows the UAV to land without damaging the net.

Once assembled, the net weighs 0.948 kg and has an overall area of 0.194 m<sup>2</sup>, with the spacer occupying 0.0325 m<sup>2</sup>. This makes the effective net area 0.161 m<sup>2</sup>.

### 3.2.3 Screen location

The UAV carries the bug-zapping screen, which is suspended by paracord rope at each corner. The location of this screen determines the efficacy of the mosquito UAV, measured in mosquitoes detected per second of flight time. The following describes a simplified analysis to optimize the screen location.

For manufacturing ease, the electrified screen is a rectangle with a width of  $d_s$ . The screen is suspended a distance  $h_s$  beneath the UAV flying at height  $h_d$ . We chose to suspend the screen beneath the UAV to avoid the weight of the rigid frame that would be required if the screen were above the UAV and because most mosquito species prefer low flight [53]. This screen can be suspended at any desired angle  $\theta$  in comparison to horizontal, as shown in Fig. 3.1. Two key parameters are the distance  $h_s$  and the optimal angle  $\theta$ . The goal is to clear the greatest volume of mosquitoes per second, a volume defined by the UAV forward velocity  $v_f$  and the cross-sectional area  $h_m \times d_s$  cleared by the screen, as shown in Fig. 3.2.

To hover, the UAV must push sufficient air down with velocity  $v_d$  to apply a force that cancels the pull of gravity. The UAV and screen combined have mass  $m_d$  and its cross section can be approximated as a square with a side length of  $d_d$ . The mass flow of air through the UAV's propellers is equal to the product of the change in velocity of the air, the density of the air  $\rho_a$ , and the cross sectional area.

We assume that air above the UAV is quiescent, so the change in velocity of the

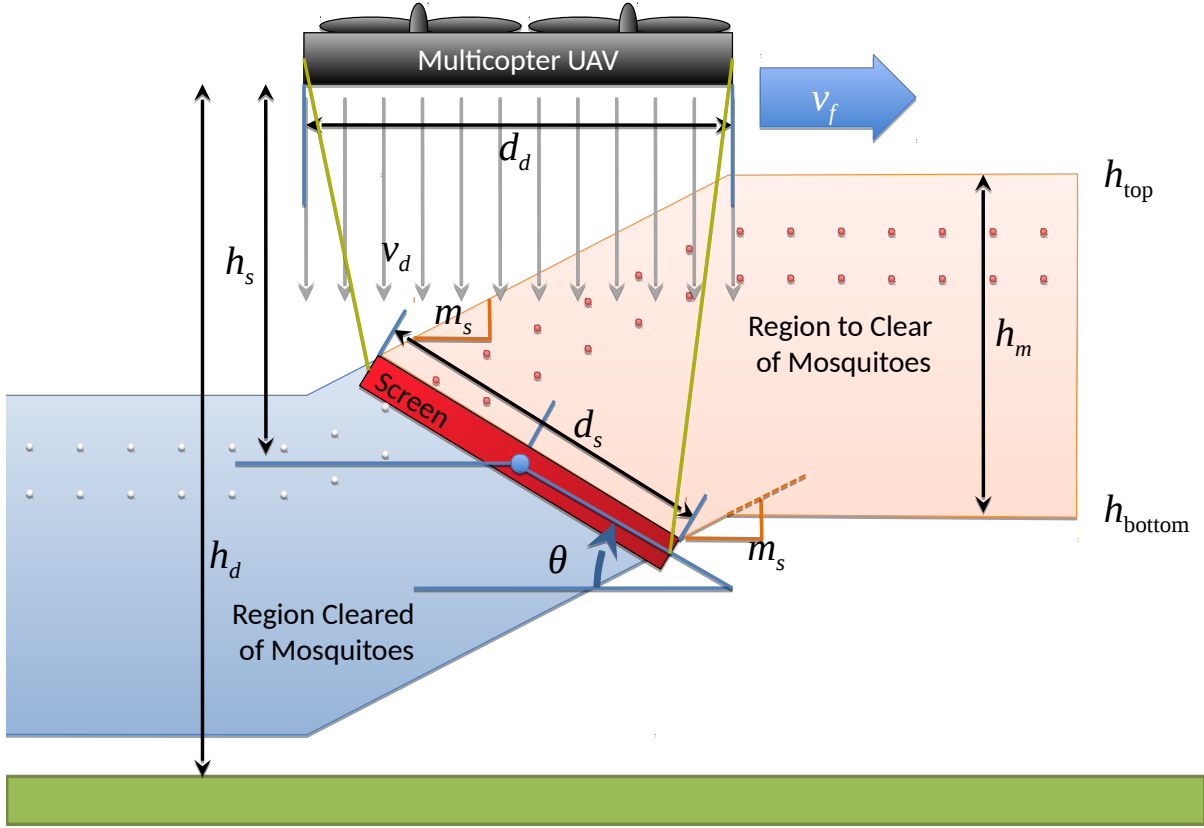


Figure 3.1: Propwash pushes incoming mosquitoes downwards, and the UAV clears a volume  $h_m d_s v_f$  each second. Circles show two mosquitoes at equal time intervals relative to the UAV.

air is  $v_d$  m/s. So that

Force gravity = (mass flow) air velocity and

$$m_d g = (v_d \rho_a d_d^2) v_d. \quad (3.1)$$

Then the required *propwash*, the velocity of air beneath the UAV, for hovering is

$$v_d = \sqrt{\frac{m_d g}{\rho_a d_d^2}}. \quad (3.2)$$

The flight testing site in Houston, Texas is 15 m above sea level. At sea level the density of air  $\rho_a$  is  $1.225 \text{ kg/m}^3$ . The UAV and instrumentation combined weigh 5.1 kg with a width of 0.75 m. The acceleration due to gravity is  $9.871 \text{ m/s}^2$ . Substituting these values gives  $v_d = 8.5 \text{ m/s}$ .

Due to propwash, an initially hovering mosquito will fall when under the UAV at

a rate of  $v_d$ . Relative to the UAV, the mosquito moves horizontally at a rate of  $-v_f$ . As shown in Fig. 3.1, we can extend lines with slope  $-v_d/v_f$  from the screen's trailing edge to  $h_{\text{top}}$  and from the leading edge to  $h_{\text{bottom}}$ .

$$\begin{aligned}
 h_{\text{top}} &= h_d - h_s + \frac{d_s}{2} \sin(\theta) + \frac{d_d + d_s \cos(\theta)}{2} \frac{v_d}{v_f} \\
 h_{\text{bottom}} &= h_d - h_s - \frac{d_s}{2} \sin(\theta) + \frac{d_d - d_s \cos(\theta)}{2} \frac{v_d}{v_f} \\
 h_m &= h_{\text{top}} - h_{\text{bottom}} = d_s \left( \frac{v_d}{v_f} \cos(\theta) + \sin(\theta) \right)
 \end{aligned} \tag{3.3}$$

The optimal angle is therefore a function of forward and propwash velocity:

$$\theta = \arctan \left( \frac{v_f}{v_d} \right). \tag{3.4}$$

To ensure the maximum number of mosquitoes are collected, the screen must be sufficiently far below the UAV  $h_s > \frac{d_s}{2} \sin(\theta) + \frac{d_d + d_s \cos(\theta)}{2} \frac{v_d}{v_f}$  and the bottom of the screen must not touch the ground,  $h_d > h_s + \frac{d_s}{2} \sin(\theta)$ .

There are practical limits to  $h_s$  as well. Tests with  $h_s > 2$  m were abandoned because the long length caused the screen to act as a pendulum, introducing dynamics that made the system difficult to fly.

Changing the flying height  $h_d$  of the UAV will target different mosquito populations because mosquitoes are not distributed uniformly vertically. Gillies and Wilkes demonstrated that different species of mosquitoes prefer to fly at different heights [53].

### 3.2.4 Wind tunnel verification of net angle

This section describes experiments run in a wind tunnel to verify the simplified net angle analysis in the previous section. Smoke streaklines were used to visualize the flow of air as it passed by the UAV. Due to space constraints in the wind tunnel, a free-flying phantom 4 was used instead of the hexacopter used for carrying the zapper. The wind

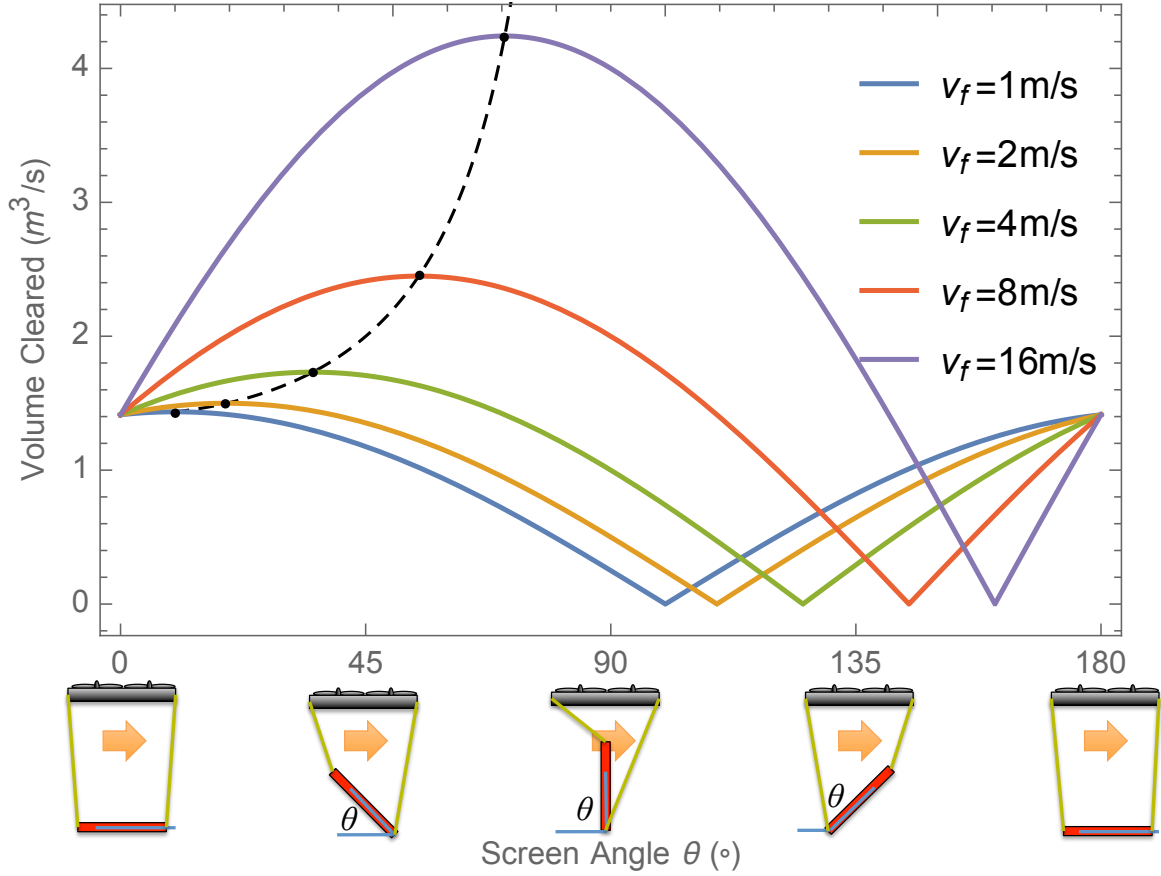


Figure 3.2: The volume cleared by a UAV is a function of screen angle  $\theta$  and forward velocity  $v_f$ . Dotted line shows the optimal angle given in (3.4)

tunnel was set to a 3 m/s flow speed, and the UAV manually flown in approximately stable hovering. The solo UAV is  $0.3 \times 0.3 \times 0.2$  m. The windtunnel has a  $1 \text{ m} \times 1 \text{ m}$  cross section. As seen from Fig. 3.3, the proposed screen position captures free flowing air and air entrained by the UAV propellers. This test encouraged us to mount the net as close to the UAV as possible, so that air, and flying mosquitoes, entrained by the propellers are pushed into the net [13].

### 3.2.5 Data logger

The electrical detection and logging system is powered by a 9 V lithium ion battery applied directly to the controller and two AA 3 V lithium ion batteries applied to the

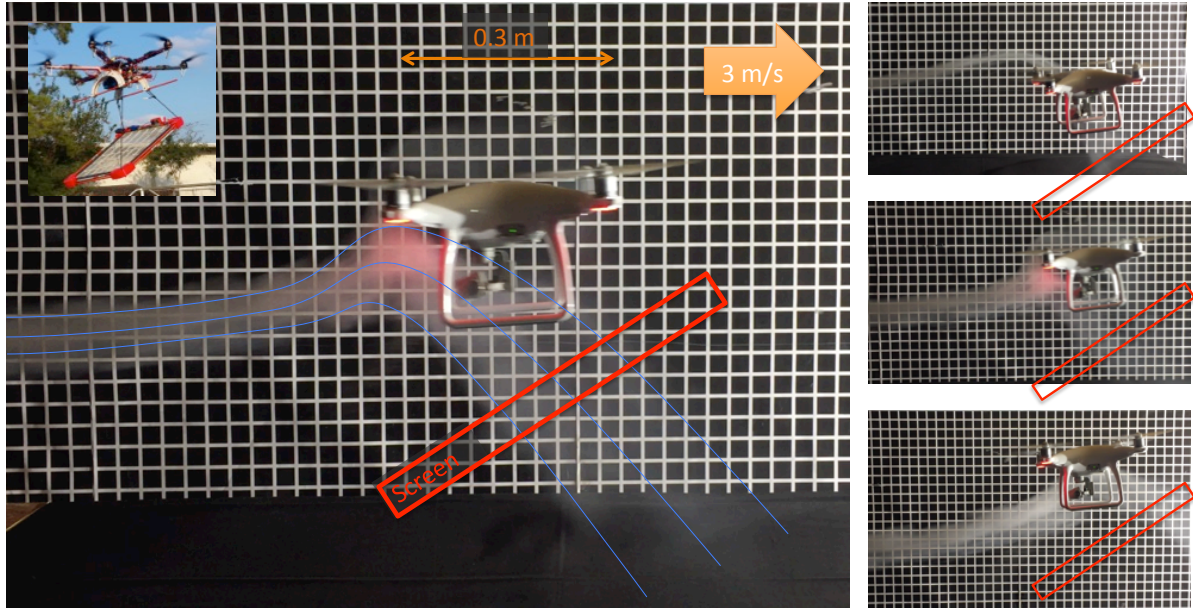


Figure 3.3: Frames from wind tunnel test with free-flying UAV at 3 m/s windspeed with smoke for streaklines. Each black square is 25.4 mm in width.

power circuit for the screen. The controller uses a GPS shield for monitoring the location and altitude as well as a real time clock to timestamp each data point collected from the system. A Raspberry Pi 3 is used for data logging, sensors include a GPS sensor (NEO-6M Ublox), a capacitive humidity sensor, a thermistor (DHT22), and an INA219 high side, 12-bit DC current sensor for monitoring the supply-side current delivered to the net. The net current draw is logged at 100 Hz, while GPS and weather sensor data is logged at 1Hz. All data is stored on an onboard SD card.

### 3.2.6 Energy budget

Tests with an oscilloscope show that in the steady state, a 30.5 cm  $\times$  61 cm screen and electronics have a power consumption of 3.6 W. During a zap, the screen voltage monitoring circuit shorts briefly when the mosquito contacts the screen. Figure 3.4 shows the time sequences for battery and screen voltages, current, and power during five mosquito zaps. Multiplying voltage by current to find the instantaneous power ( $p = iv$ ) and integrating the area under the power curve show a total energy consumption of

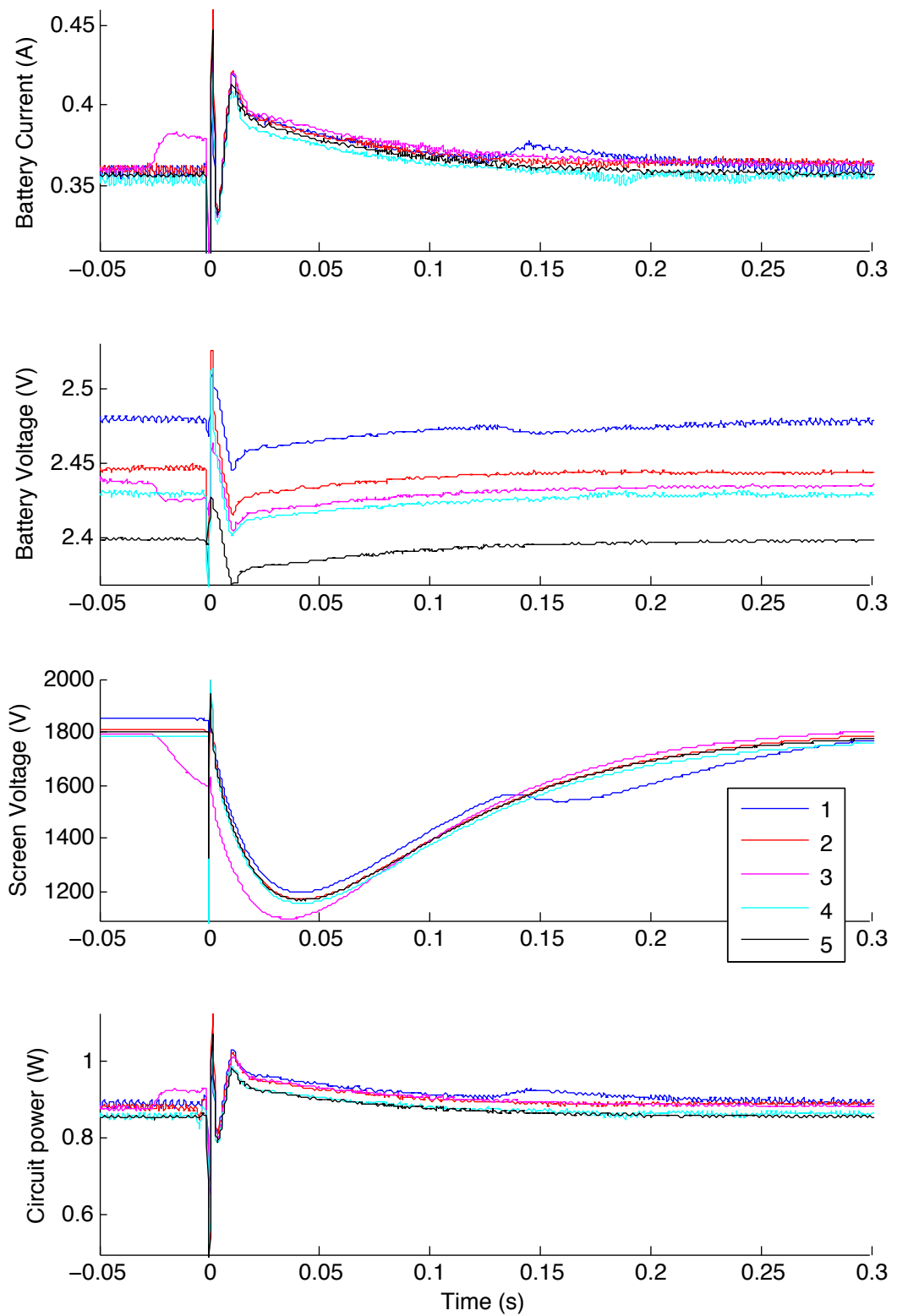


Figure 3.4: Current, voltage, and power traces for five *Culex quinquefasciatus* mosquitoes as each contacts the bug-zapping screen at  $t = 0$ . Contact causes a brief short that recovers in 160 ms.

4.2 mJ for each zap. Recharging the screen requires more power and is represented in the latter part of the curves. The overall recovery time is about 160 ms. Most of the energy is consumed charging and maintaining the charge on the screen rather than in zapping the mosquitoes.

### 3.3 Planning minimal turn cost paths

#### 3.3.1 Modelling mosquito density

Due to a-priori knowledge of mosquitoes' preferred habitats from entomology, we can model the density of mosquitos in a field we want to cover. This knowledge will help us plan the most efficient path, killing the most mosquitoes with the least amount of energy used. First, we divide a field for coverage into a pixel grid, the size of each pixel dictated by the size of the net and the resolution of the UAV's GPS. Each pixel  $p_i \in P$  we give a relative density value  $c(p_i)$  that describes the estimated mosquito density based on the environmental factor of the pixel. In  $P$  there will only be a subset with high relative density value. The goal is to maximize the density covered by the set  $S \subseteq P$  of visited pixels i.e.,  $\max_{S \subseteq P} \sum_{p_i \in S} c(p_i)$  within the available battery capacity. This could be done in one single trip or over multiple trips with multiple batteries.

#### 3.3.2 Turn Cost

UAVs can make turns on the spot, without curvature constraints like a fix-winged aircraft. However, UAVs turns are energetically expensive. As Fig. 3.5 shows, the energy required per meter of travel in a turn is 4 to 5 times as expensive as traveling through a straight path. The limiting factor for a UAV's flight is its battery capacity, therefore it is important to limit the amount of turns needed per flight while maximizing the amount of pixels visited. To consider the total energy cost of a turn, we need to limit the types of turns the UAV made. We consider only strict set of  $90^\circ$  and  $180^\circ$  turns since the UAV

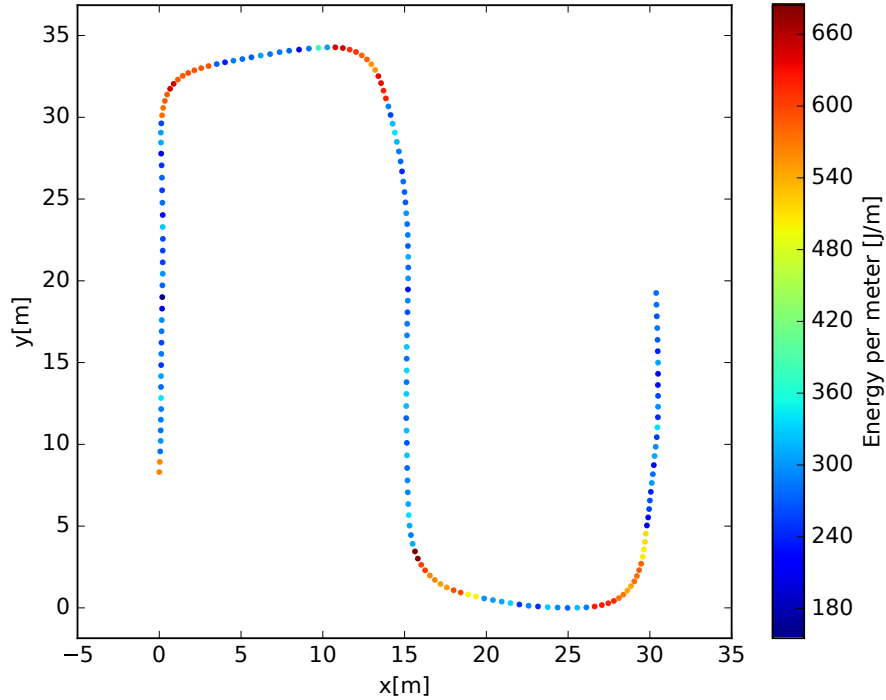


Figure 3.5: Turns are expensive. See our related video at <https://youtu.be/SFy0MDgdNao> for details, and [54] for an accompanying abstract.

does not have minimal turn curvature. Additionally, the two turn angles allow us to fly around most large obstacles while visiting the pixels around it.

### 3.4 Experiments

The results for representative flights are described below. Figure 3.6 compares the energy consumption for three coverage schemes for a region including a large obstacle in the center. A boustrophedon path requires 50 turns, 187kJ, 160s, and 181m. A hand-designed path requires 45 turns, 214kJ, 155s, and 178m. A path computed using the optimal penalty cycle cover requires only 33 turns, 184kJ, 133s, and 176m.

A boustrophedon (back-and-forth) path with 2m spacing was generated to cover a region  $120\text{ m} \times 15\text{ m}$  at height 1.5m. The path was generated using Mission Planner software from ardupilot.org [55].

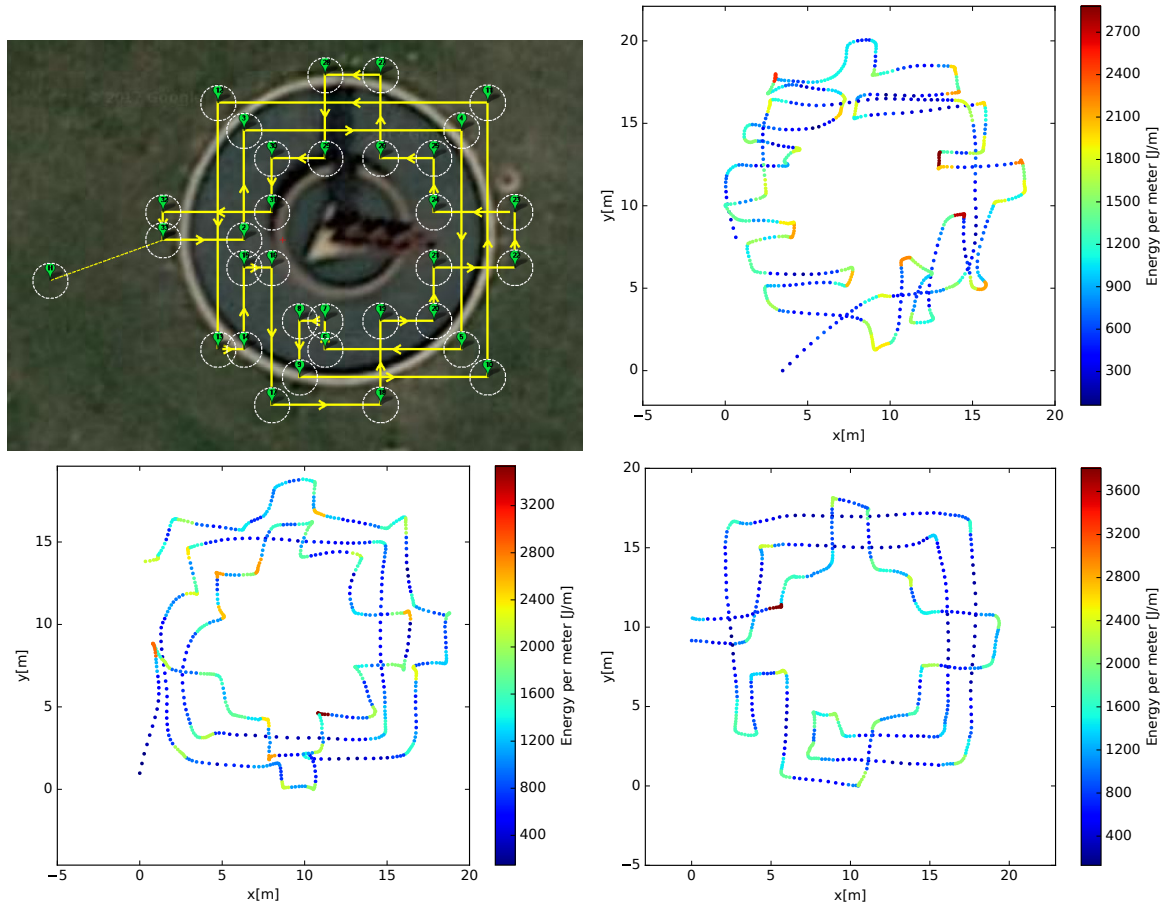


Figure 3.6: Paths and energy required for an environment surrounding an obstacle. a) optimal penalty cycle cover path. Energy required for b) a boustrophedon path, c) a loop path, d) the optimal path.

For each trial the UAV took off from a resting position on top of the screen. Flight began manually, with a piloted takeoff of the UAV. After establishing a stable hover at 3 m, control was switched to the autonomous flight plan. The pilot monitored the flight with the ability to switch to manual operation in case of potential crashes due to GPS error or hazards in the flight plan. Mosquito strikes detected by the data logger were verified using a GoPro Hero 4 Silver camera attached at the top of the net, as shown in Fig. 1.2. At night and twilight, the sparks could be detected both visually and audibly from the recorded video. During the day, the sparks were loud enough to observe over the audio channel of the videos.



Figure 3.7: The UAV’s path for flight 3 is in red. Strikes collected along this path are represented by yellow dots.

The UAV flew eight missions on this field, covering the same path. It was mainly flown in the early morning and late afternoon, when mosquito activities are more active. Three flights were flown at noon and early afternoon to ensure that mosquito activities during these periods were not ignored. However, only two mosquito strikes were observed during this period. The path covered is about 1 km long and typically takes 12 min.

Over the eight missions on this field, there were a total of 11 mosquito strikes. Figure 3.7 shows the mission’s flight path and the map of all collected strikes. The mosquito strikes are concentrated at the north and south ends of the field, where there are more trees. A density map was generated from the collected strikes’ position by representing each strike by a Gaussian distribution with the norm on the strike’s location and a  $\sigma$  of 10 m. Figure 3.8 shows the density map generated by summing these Gaussian distributions.

These results not only tell where mosquitoes were but also show where mosquitoes were not. This is a key difference from stationary traps such as [11, 12]. Figure 3.9 shows the UAV during a dawn flight test near the ocean.

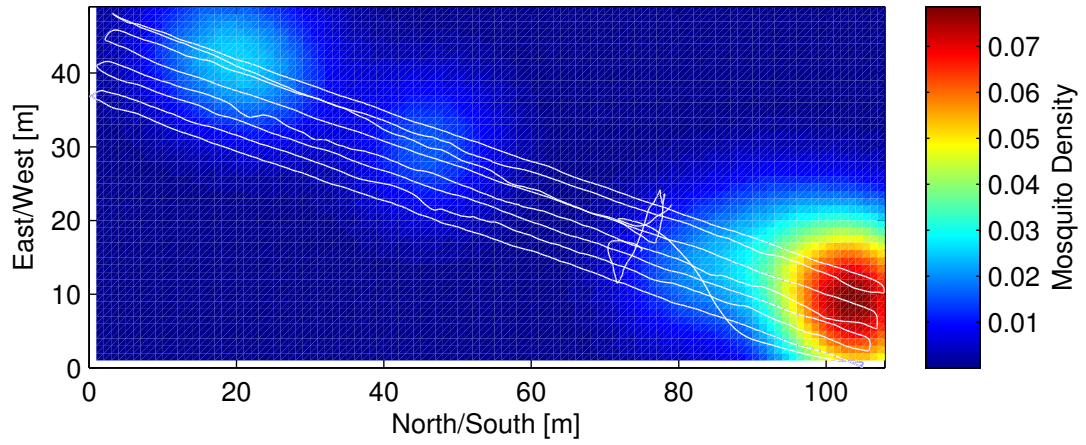


Figure 3.8: Density map showing mosquito distribution on the field, overlaid by flight path 4 in white.



Figure 3.9: The UAV and screen during a flight trial near the ocean.

### 3.5 Conclusion and future work

This chapter presented an approach for finding optimal tours given turn costs and an energy budget, inspired by a mosquito-killing UAV with limited battery life. Initial experiments with the UAV and electrified screen track the location of a mosquito-killing UAV as it patrols a field and maps mosquito kills.

Many refinements to the algorithm could be pursued in future work, including changes to both the mosquito-biasing algorithm and the robot flight simulation. The model may be expanded to continuous space, three dimensions, and to arbitrary turn angles. These and other considerations will make a more realistic model for future work.

Further testing of the multi-copter UAV is indicated and will allow more extensive testing of the robustness and accuracy of the hardware design. New sensors that can identify and detect flying insects [11] may be added to the UAV and enable it to proactively steer toward insect swarms and identify insects in realtime.

The concept may be extended to a non-destructive population survey in which the screen could be replaced with a net and, with appropriate lighting, the camera used to record capture events. Teams of UAVs could work together to map areas more quickly and, by measuring gradients of the distribution, quickly find large mosquito populations.

## Chapter 4

# Surveying underwater with drifting sensor network

### 4.1 Driftnode design

#### 4.1.1 Hardware



Figure 4.1: a) driftnode sensor cap. Threaded to the bottom of the driftnode. With turbidity, pressure and range sensor attached. b) bottom of driftnode sensor cap coated with rubber silicone.

You can see the driftnode's shell and electronics in Fig. 1.3. The current driftnode shell is an improvement upon the driftnode from [14]. It is composed of a 43 cm PVC pipe, with a 3D-printed male-threaded bushing glued to top and bottom of the pipe. The glue joints and exterior surfaces of the male threaded bushing are coated with a rubber silicone coating for waterproofing. The driftnode's bottom and top caps can be threaded on to the threaded bushing on the pipe, completing the exterior of the drift node. The bottom cap has sensors incorporated. After the sensors are installed, the exterior surfaces of the cap are coated in the same rubber silicone coating as seen in Fig. 4.1. The sensors used are all waterproof for their sensing elements. The threaded

sensor and top caps allow easy removal of the inside electronics and sensor for charging, debugging and improvement.

The driftnode's primary electronics include a Raspberry Pi 3 embedded computer for logging sensor data and broadcasting the wireless access point. The Raspberry Pi 3 is powered by a 10 Ah portable USB battery. We used a proto-hat on the Raspberry Pi to facilitate easy connection to sensors.

The driftnode can record its position with a commercially available GPS unit, in this case, it is the Adafruit Ultimate GPS Breakout board, connected to an extended GPS antenna. The GPS sensor talks to the Raspberry Pi via serial communication. We can record the orientation of the driftnode with a 9-axis inertial measurement unit sensor, in this case, a Pololu MinIMU-9 v5. We also have an analog turbidity sensor and a pressure sensor for the driftnode, both output analog voltages, which is then converted to digital signal by the ADS1115 16-bit ADC board by Adafruit. both the IMU and ADC board communicate to the Raspberry Pi through I<sup>2</sup>C.

We have attempted to find a suitable underwater depth sensor. We need a sensor that is small, preferably lightweight, and relatively easy to interface. However, many available depth sensors do not meet these requirements. When speaking of underwater depth sensing via distance, fish finder sensors come to mind. These sensors also output a point cloud similar to LIDAR sensor or depth cameras. However, we have not been able to find a resource to interface with them quickly. All commercially available fish finder sensors are coupled with either a visualizer or communicate with proprietary visualizing software. Another member of our lab is working on reverse engineering fish finder sensors. Fish finders are also typically larger than the area available in our sensor cap. We have found two sensors, with a compromise on accuracy. One is the MB7380 by MaxBotix, which is a weatherproofed sonar sensor that could be further waterproofed then incorporated into our driftnode. The second sensor is a JSN-SR04T based sonar

sensor with a sonar probe connected by a waterproof cable. These two sensors were designed to be used in the air, with the waterproofing feature intended to make them more reliable outdoor. However, we retrofitted them to work underwater, taking into account that the speed of sound in water is 1498 m/s, four times faster than the speed of sound in air 343 m/s.

We left out the camera since our testing environment has very murky water. Additionally, our turbidity, pressure, and range sensors have taken up most of the area of the sensor cap. Which can be added back in at a later date when we have a wider area for our sensor cap, or possibly a transparent tube which allow us to mount the camera facing to the side.

#### 4.1.2 Software

The Raspberry Pi 3 is installed with embedded Linux operating system Raspbian. Raspbian is based on Debian, which can run a simple version of the Robotics Operating System (ROS). ROS allows us to communicate between multiple software nodes hosted on multiple computers. This means we can easily connect one drift node to another, or a driftnode to a data collecting embedded computer carried on an AUV.

All sensors are logged using ROS bag files. Each sensor has its own Python script file that publishes on a topic for that sensor. The GPS data is published with *sensor\_msgs/NavSatFix* messages. The IMU data is published with *sensor\_msgs/IMU* messages. The turbidity data is published with *sensor\_msgs/Illuminance* messages. The range data is published with *sensor\_msgs/Range* messages. The pressure data is published with *sensor\_msgs/FluidPressure* messages. Because ROS messages are recorded with publishing time and host name, sensor messages can be played back synchronously.

Fig 4.2 shows visualizations for the GPS trace and the IMU data. The GPS trace can be graphed by an online GPS visualizer, such as <http://www.gpsvisualizer.com/>. The

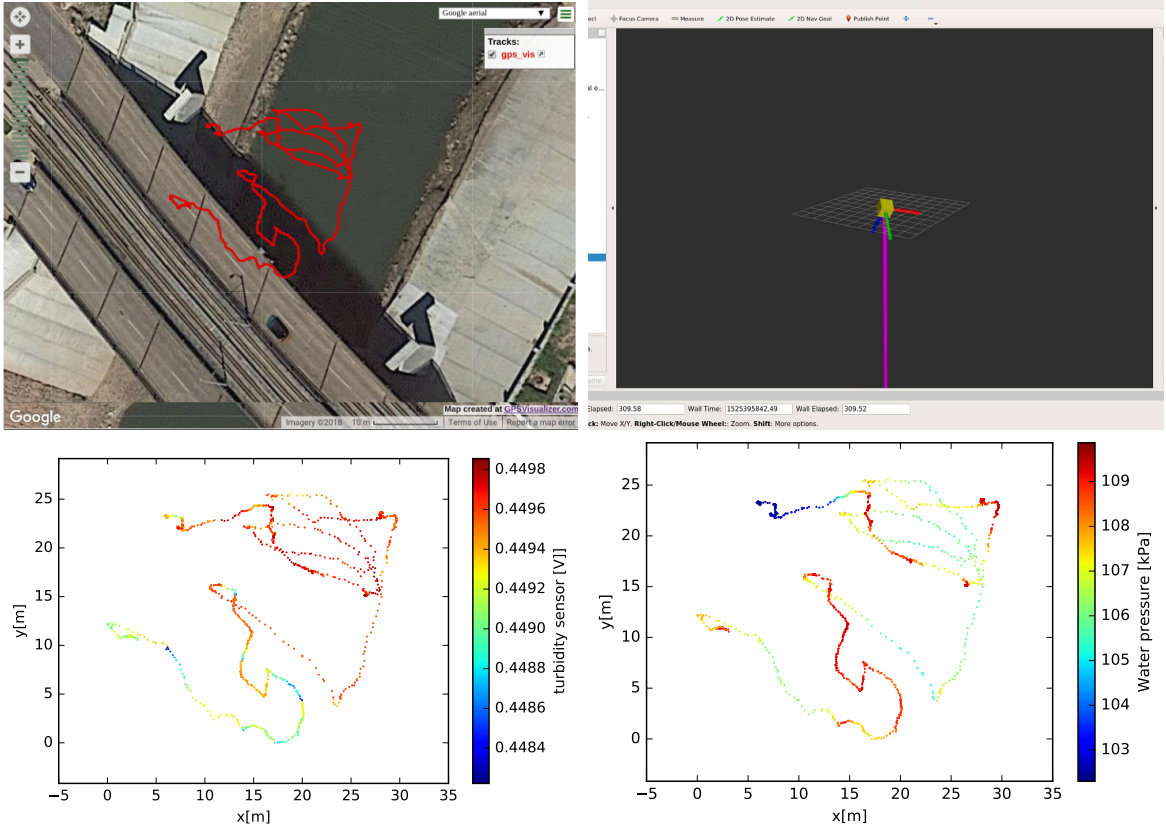


Figure 4.2: a) GPS trace of a drift node mission. b) IMU data visualized using Rviz, showing the orientation of the drift node. c) Turbidity sensor data overlaid on top of the GPS trace. d) Pressure sensor data overlaid on top of the GPS trace.

IMU data is visualized to show the orientation of the drift node, using Rviz, a ROS tool. The other data streams can be overlaid on to the GPS trace.

## 4.2 Testing driftnode

### 4.2.1 Commercially available depth transducer

Extensive testing were done to find a suitable depth sensor for a small, lightweight sensor node with data logging and transmitting. The first sensors considered were commercially available sonar depth sensor designed for large and small fishing boats, such as the Garmin GDT 43 depth and temperature transducer. However, most of these



Figure 4.3: a) Garmin GDT 43 uses NMEA 2000 b) MaxBotix MB7380 use analog voltage output c) JSN-SR04T use trigger and echo timing d) Deeper Smart Sonar PRO proprietary fish finder

transducer are too large for our applications. The largest obstacle is their communication protocol, most new, "small and light weight" transducers use the NMEA 2000 communication protocol. This is a CAN Bus based protocol that is largely closed source and require extensive reverse engineering to use. There are some open sourced projects who are can inteprete these protocols, through exhaustive reverse engineering and public information. To name a few: *openskipper.org*, *KBox*, *signalk.org* and *CAN Boat* on *github.com*. However, they require additional hardware that would further weigh down our sensor nodes and ultimately will not fit within the shell.

Another sonar depth transducer intended for boats, the Cruz Pro ATU120A uses the NMEA 0183 protocol, which is a high voltage serial protocol, can possibly be used. The high voltage protocol is simple to integrate and use, requiring minimal additional hardware to interface with the Raspberry Pi. However, the size and weight of the sensor

make it hard to fit the sensor along with other packages, especially when other smaller, lightweight sensors were being investigated at the same time.

One smaller, lightweight sensor that is not designed to be used underwater but is weatherized, is the MaxBotix MB7380. The MB7380 is intended to be used in outdoor application and is therefore waterproof, even though further waterproofing were needed to be used in underwater applications. A few tutorials online exist that show how to prepare the sensor for underwater applications. However, MaxBotix's own manual show that underwater sensing are not recommended, and do not guarantee any performance metric if used as such. The MaxBotix can be interfaced with either serial protocol, or an analog voltage output, both already exist on our sensor node. Early testing in shallow water indicated that the sensor can return readings, but for real testing, we needed to take the sensor out to deeper water. This is due to the higher speed of sound in water, increasing the sensor's minimum distance.

Recently we investigated a JSN-SR04T based weatherized sensor, also intended for in air measurement but can be further waterproofed. Bakar et al. [56] showed that you can use this sensor for underwater sensing, albeit with a lot of noise that was hard to filter out. The sensor uses a timing protocol that directly excite the transducer and receiver, measuring the pulse's timing directly.

In parallel to testing sensors that can be quickly interfaced, another researcher is also attempting to reverse engineer commercially available, handheld wireless fish sensors. One example is the Deeper Smart Sonar PRO+ fish finder, shown in Fig 4.3 along with other sonar sensors.

#### 4.2.2 Testing sonar sensors

*MaxBotix sensor:*

Since we needed a mobile testing platform for our range sensors, a driftnode pro-

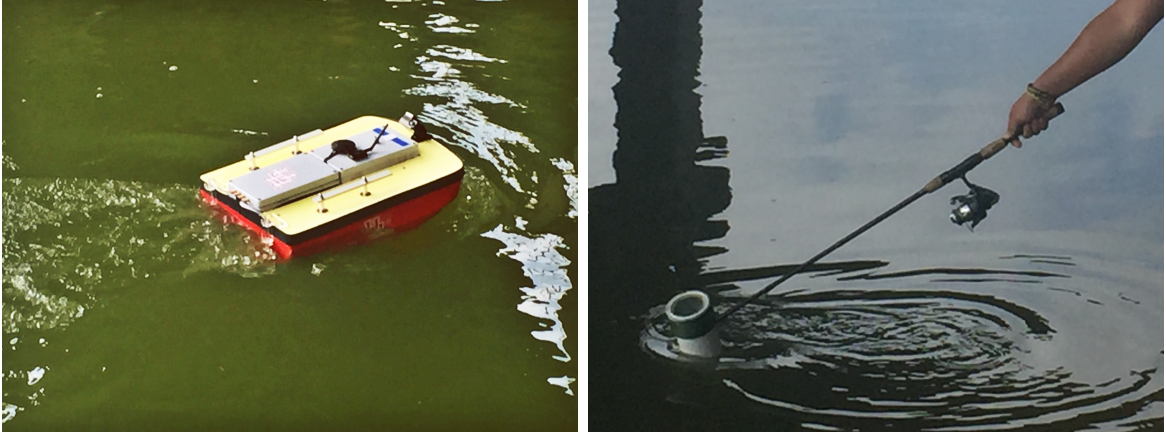


Figure 4.4: Testing the driftnode by towing the waterproof assembly behind a remote controlled boat

prototype was built that can accept different sensor caps. The Maxbotix MB7380 was integrated to the driftnode's first prototype, to test its capabilities in real world condition. As shown in Fig. 4.4 we towed the driftnode assembly while it is logging data behind a remote controlled boat for the first test. Our first test of the sensor showed that the sensor can differentiate between being submerged and in the air. Fig. 4.5 show the log file for the Maxbotix sensor, showing two distinct type of readings, where the lower, flatter reading is out of the water, and the higher, more variable reading is in the water. However, the first test did not have another sensor that we know would work to measure depth, therefore we could not compare the Maxbotix sensor against a ground truth.

The second test was to compare the sensor against a know ground truth. We used a commercially available handheld wireless fishfinder, the Venterior VT-FF001 Portable Fish Finder, to compare against the MaxBotix sensor. Ground anchors were established on each of the bayou's banks, opposite each other, where pulleys were attached and a string connecting the pulleys. The sensors were pulled along the line for a repeatable path. The fish finder data was used to compare against the MaxBotix sensor.

Fig. 4.6 show the second test's setup and a picture of the bottom of the bayou obtained with the fishfinder sensor. Fig. 4.7 show that the MaxBotix sensor returned

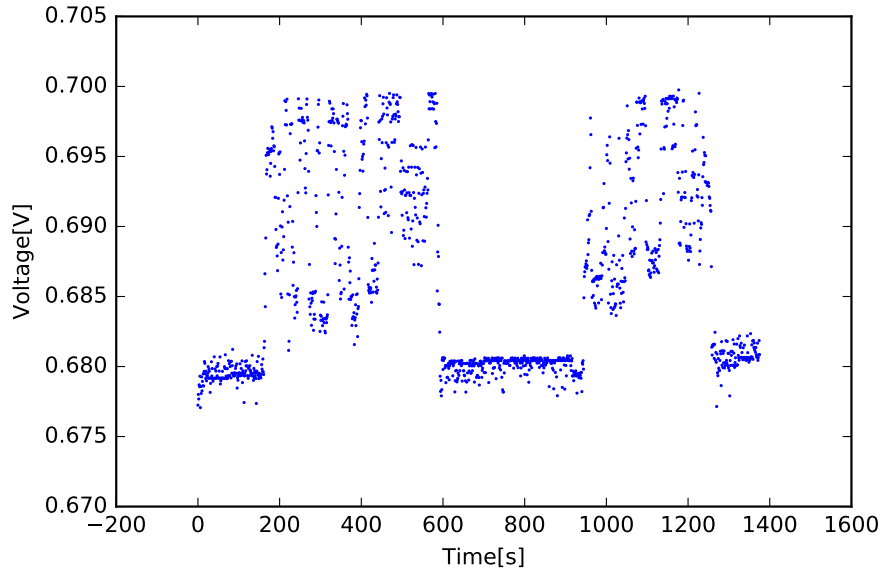


Figure 4.5: Range sensor log of the first test

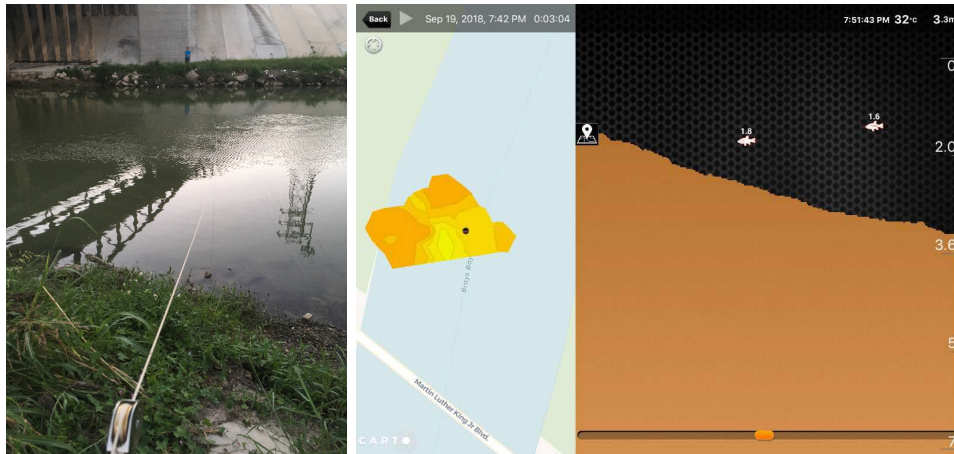


Figure 4.6: a) testing set up for the second test of MaxBotix sensor b) output of the fish finder sensor

data that was purely noise. The second test showed that the MaxBotix is not usable as an underwater depth sensor.

*JSN-SR04T waterproof sensor:*

The JSN-SR04T sensor seen in Fig. 4.3 is a basic, hobbyist level weatherized range sensor that have been shown to be capable of underwater depth sensing [56]. Fig. 4.8 show

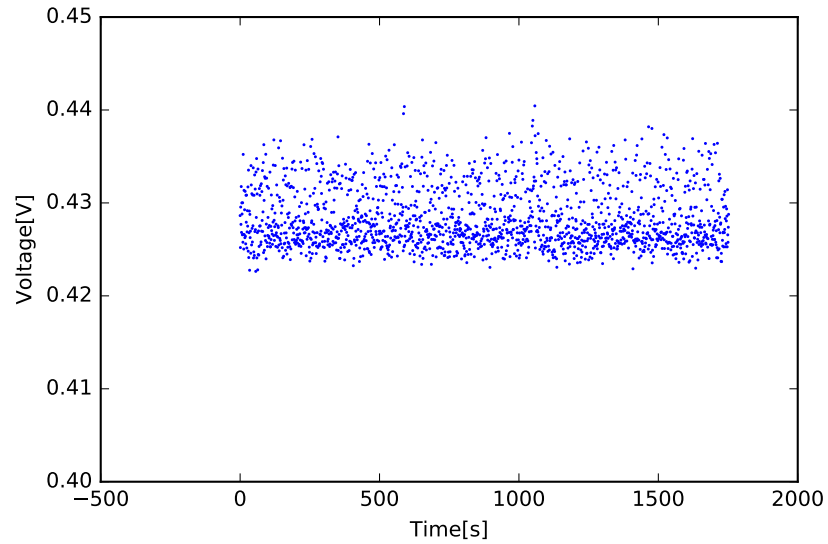


Figure 4.7: Maxbotix data log for the second test, noisy data that seems to be only noise



Figure 4.8: JSN-SR04T testing platform

the pole the sensor is attached to so that the sensor can be submerged at predetermined level. The sensor timing diagram is shown in Fig. 4.9. The sensor is attached to the end of a 1.15 m tall pole, which will allow the sensor to be submerged at a predetermined depth. During testing, the pole was submerged into a 3.35 m deep pull, and every 15 s the sensor was submerged 10 cm deeper. Fig. 4.10 show the log with of the sensor with

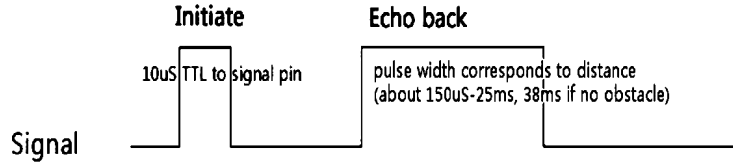


Figure 4.9: Example signal of JSN-SR04T operation

respect to time. A downward trend is clearly shown, with the maximum reading at 65 cm, and minimum reading without noise is 40 cm. This correspond to an air distance of 2.84 m maximum and 1.7 m minimum.

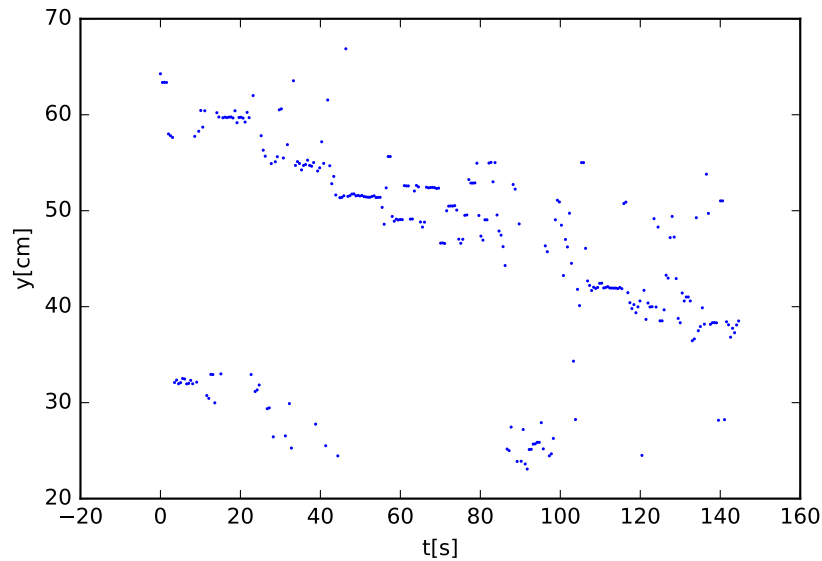


Figure 4.10: Log of the new sensor clear show a descending trend

### 4.3 Conclusion and future work

The drifting sensor node we presented can be deployed as a wireless sensor network. The driftnodes can be deployed on coastlines to gather information before a military mission. It can also be used to monitor national ocean borders or marine habitats.

For depth sensing, the commercially available fish finding transducer can be used with current open source software to communicate in NMEA 2000. In environments with

better water clarity, we can add a camera to the driftnode for more information.

Another researcher is also working on making the driftnode smaller and lighter. This would allow researchers to transport more sensors, and easier for an AUV to recover the sensor at the end of the mission.

## Chapter 5

### Conclusion

In this thesis, three applications for autonomous unmanned vehicles were presented. Unmanned aerial vehicles (UAV) can be used to deploy, retrieve geophones for seismic surveying and deploy unmanned rover attached with geophones. We presented software to plan for a wireless sensor network deployment using UAV and unmanned rover. A UAV was used to drag an electrified net through an area to destructively survey mosquito populations. We used our collaborator's algorithm to reduce the energy expenditure while maximizing area covered. An updated design for drifting wireless sensor node was presented. The drift node can be used to survey coastlines and national maritime boundaries for marine border security, wildlife science missions.

In future work, the applications above could be merged together for a more complete package. A wireless sensor network can then be deployed, monitored and retrieved by AUVs. Before the WSN deployment, the area can be surveyed by a UAV with minimal energy expenditure. Wireless sensor nodes can communicate with each other to relay position, cache data or relay data back to the base station. Like in [57], UAVs can monitor data and charge wireless sensor nodes, extending their longevity. For destructive mosquito surveying methods, the UAVs can incorporate live data to plan its route reactively.

## References

- [1] G. Werner-Allen, K. Lorincz, M. Ruiz, O. Marcillo, J. Johnson, J. Lees, and M. Welsh, “Deploying a wireless sensor network on an active volcano,” *IEEE internet computing*, vol. 10, no. 2, pp. 18–25, 2006.
- [2] D. Dominici, V. Baiocchi, A. Zavino, M. Alicandro, and M. Elaiopoulos, “Micro UAV for post seismic hazards surveying in old city center of L’Aquila,” in *Proceedings of the FIG Working Week*, 2012, pp. 06–10.
- [3] K. Nagatani, K. Akiyama, G. Yamauchi, H. Otsuka, T. Nakamura, S. Kiribayashi, K. Yoshida, Y. Hada, S. Yuta, K. Fujino, T. Izu, and R. Mackay, “Volcanic ash observation in active volcano areas using teleoperated mobile robots - introduction to our robotic-volcano-observation project and field experiments,” in *2013 IEEE International Symposium on Safety, Security, and Rescue Robotics (SSRR)*, Oct 2013, pp. 1–6.
- [4] Q. Wu, N. S. Rao, X. Du, S. S. Iyengar, and V. K. Vaishnavi, “On efficient deployment of sensors on planar grid,” *Computer Communications*, vol. 30, no. 14, pp. 2721–2734, 2007.
- [5] V. Dyo, S. A. Ellwood, D. W. Macdonald, A. Markham, C. Mascolo, B. Pásztor, S. Scellato, N. Trigoni, R. Wohlers, and K. Yousef, “Evolution and sustainability of a wildlife monitoring sensor network,” in *Proceedings of the 8th ACM Conference on Embedded Networked Sensor Systems*. ACM, 2010, pp. 127–140.
- [6] A. Mainwaring, D. Culler, J. Polastre, R. Szewczyk, and J. Anderson, “Wireless sensor networks for habitat monitoring,” in *Proceedings of the 1st ACM international workshop on Wireless sensor networks and applications*. ACM, 2002, pp. 88–97.

- [7] C. J. Murray, L. C. Rosenfeld, S. S. Lim, K. G. Andrews, K. J. Foreman, D. Haring, N. Fullman, M. Naghavi, R. Lozano, and A. D. Lopez, “Global malaria mortality between 1980 and 2010: a systematic analysis,” *The Lancet*, vol. 379, no. 9814, pp. 413–431, 2012.
- [8] J. E. Parker, N. Angarita-Jaimes, M. Abe, C. E. Towers, D. Towers, and P. J. McCall, “Infrared video tracking of anopheles gambiae at insecticide-treated bed nets reveals rapid decisive impact after brief localised net contact,” *Scientific Reports*, vol. 5, 2015.
- [9] S. Butail, N. Manoukis, M. Diallo, A. S. Yaro, A. Dao, S. F. Traoré, J. M. Ribeiro, T. Lehmann, and D. A. Paley, “3d tracking of mating events in wild swarms of the malaria mosquito anopheles gambiae,” in *2011 Annual International Conference of the IEEE Engineering in Medicine and Biology Society*. IEEE, 2011, pp. 720–723.
- [10] G. M. Williams and J. B. Gingrich, “Comparison of light traps, gravid traps, and resting boxes for west nile virus surveillance,” *Journal of Vector Ecology*, vol. 32, no. 2, pp. 285–291, 2007.
- [11] Y. Chen, A. Why, G. Batista, A. Mafra-Neto, and E. Keogh, “Flying insect classification with inexpensive sensors,” *Journal of Insect Behavior*, vol. 27, no. 5, pp. 657–677, 2014.
- [12] A. Linn, “Building a better mosquito trap,” *International Pest Control*, vol. 58, no. 4, p. 213, 2016.
- [13] S. Bhatnagar, A. Nguyen, D. Krupke, S. P. Fekete, and A. T. Becker, “UAV for destructive surveys of mosquito population (video),” Feb. 2018. [Online]. Available: <https://youtu.be/OTQSR03Bv5g>

- [14] D. Boydstun, M. Farich, J. M. III, S. Rubinson, Z. Smith, and I. Rekleitis, “Drifter sensor network for environmental monitoring,” in *2015 12th Conference on Computer and Robot Vision*, June 2015, pp. 16–22.
- [15] S. K. V. Sudarshan, V. Montano, A. Nguyen, M. McClimans, L. Chang, R. R. Stewart, and A. T. Becker, “A heterogeneous robotics team for large-scale seismic sensing,” *IEEE Robotics and Automation Letters*, vol. 2, no. 3, pp. 1328–1335, July 2017.
- [16] S. K. V. Sudarshan, L. Huang, C. Li, R. Stewart, and A. T. Becker, “Seismic surveying with drone-mounted geophones,” in *CASE, 12th Conference on Automation Science and Engineering*. IEEE, 2016, pp. 1–6.
- [17] G. W. Wood, R. L. Workman, and M. W. Norris, “Distributed seismic data-gathering system,” Mar. 3 1998, US Patent 5,724,241.
- [18] J. Jiang, A. A. Aziz, Y. Liu, and K.-M. Strack, “Geophysical data acquisition system,” Jun. 16 2015, US Patent 9,057,801.
- [19] Goins, Neal Rodney, A. M. Dainty, and M. N. Toksz, “Lunar seismology: The internal structure of the Moon.” in *Journal of Geophysical Research: Solid Earth* 86.B6, 1981, pp. 5061–5074.
- [20] Jean-Jacques Postel, Thomas Bianchi, Jonathan Grimsdale, “Patent us20140307525: Drone seismic sensing method and apparatus,” October 2014. [Online]. Available: <https://www.google.com/patents/US20140307525>
- [21] E. Coste, K. E. Welker, and G. D. Tamboise, “Seismic acquisition system-based unmanned airborne vehicle,” Sep. 13 2013, US Patent App. 14/027,094.
- [22] Mars Advanced Planning Group 2006, “Robotic mars exploration strategy 20072016,” National Aeronautics and Space Administration, Tech. Rep., March

2006. [Online]. Available: [http://mepag.jpl.nasa.gov/reports/3715\\_Mars\\_Expl-Strat\\_GPO.pdf](http://mepag.jpl.nasa.gov/reports/3715_Mars_Expl-Strat_GPO.pdf)
- [23] E. Muyzert, K. Welker, I. Cooper, S. Bittleston, L. Combee, R. Ross, and E. Kotochigov, “Marine seismic survey systems and methods using autonomously or remotely operated vehicles,” Apr. 21 2015, US Patent 9,013,952.
- [24] J.-J. Postel, T. Bianchi, and J. Grimsdale, “Drone seismic sensing method and apparatus,” Mar. 20 2014, US Patent App. 14/220,996.
- [25] S. W. Wilcox, J. C. Whelan, and J. Alexander, “Seismic data recording,” Sep. 5 2013, US Patent App. 14/018,853.
- [26] A. Howard, M. J. Matarić, and G. S. Sukhatme, “Mobile sensor network deployment using potential fields: A distributed, scalable solution to the area coverage problem,” in *Distributed Autonomous Robotic Systems 5*. Springer, 2002, pp. 299–308.
- [27] P. Corke, S. Hrabar, R. Peterson, D. Rus, S. Saripalli, and G. Sukhatme, “Autonomous deployment and repair of a sensor network using an unmanned aerial vehicle,” in *Robotics and Automation, 2004. Proceedings. ICRA’04. 2004 IEEE International Conference on*, vol. 4. IEEE, 2004, pp. 3602–3608.
- [28] G. Tuna, V. C. Gungor, and K. Gulez, “An autonomous wireless sensor network deployment system using mobile robots for human existence detection in case of disasters,” *Ad Hoc Networks*, vol. 13, pp. 54–68, 2014.
- [29] A. Howard, L. E. Parker, and G. S. Sukhatme, “Experiments with a large heterogeneous mobile robot team: Exploration, mapping, deployment and detection,” *The International Journal of Robotics Research*, vol. 25, no. 5-6, pp. 431–447, 2006.
- [30] V. B. Montano and A. T. Becker, “SeismicDart,” Sep. 2016. [Online]. Available: <http://www.thingiverse.com/thing:1713499>

- [31] T. Miyazaki, K. Mukaiyama, Y. Komori, K. Okawa, S. Taguchi, and H. Sugiura, “Aerodynamic properties of an archery arrow,” *Sports Engineering*, vol. 16, no. 1, pp. 43–54, 2013.
- [32] S. K. V. Sudarshan and A. T. Becker, ““Seismic Survey Scheduler.” MATLAB Central File Exchange,” Sep. 2016. [Online]. Available: <http://www.mathworks.com/matlabcentral/fileexchange/59034>
- [33] K. Merz, A. G. Green, T. Buchli, S. M. Springman, and H. Maurer, “A new 3-D thin-skinned rock glacier model based on helicopter GPR results from the Swiss alps,” *Geophysical Research Letters*, vol. 42, no. 11, pp. 4464–4472, 2015.
- [34] A. Nguyen, D. Krupke, M. Burbage, S. Bhatnagar, S. P. Fekete, and A. T. Becker, “Using a UAV for destructive surveys of mosquito population,” in *2018 IEEE International Conference on Robotics and Automation, ICRA 2018, Brisbane, Australia, May 21-25, 2018*, 2018, pp. 7812–7819. [Online]. Available: <https://doi.org/10.1109/ICRA.2018.8463184>
- [35] J. A. Dennett, A. Bala, T. Wuithiranyagool, Y. Randle, C. B Sargent, H. Guzman, M. Siirin, H. K Hassan, M. Reyna, T. Unnasch, R. B Tesh, R. E Parsons, and R. Bueno, “Associations between two mosquito populations and west nile virus in harris county, texas, 2003–06,” *Journal of the American Mosquito Control Association*, vol. 23, no. 3, p. 264, 2007.
- [36] R. Peter, P. Van den Bossche, B. L. Penzhorn, and B. Sharp, “Tick, fly, and mosquito control—lessons from the past, solutions for the future,” *Veterinary parasitology*, vol. 132, no. 3, pp. 205–215, 2005.
- [37] W. H. Organization, “Guidelines for laboratory and field testing of mosquito larvicides,” *World Health Organization communicable disease control, prevention and eradication WHO pesticide evaluation scheme*, 2005.

- [38] D. V. Maliti, N. J. Govella, G. F. Killeen, N. Mirzai, P. C. Johnson, K. Kreppel, and H. M. Ferguson, “Development and evaluation of mosquito-electrocuting traps as alternatives to the human landing catch technique for sampling host-seeking malaria vectors,” *Malaria Journal*, vol. 14, no. 1, p. 1, 2015.
- [39] J. M. Marshall and C. E. Taylor, “Malaria control with transgenic mosquitoes,” *PLoS Med*, vol. 6, no. 2, p. e1000020, 2009.
- [40] C. A. Hill, F. C. Kafatos, S. K. Stansfield, and F. H. Collins, “Arthropod-borne diseases: vector control in the genomics era,” *Nature Reviews Microbiology*, vol. 3, no. 3, pp. 262–268, 2005.
- [41] M. O. Ndiath, S. Sougoufara, A. Gaye, C. Mazonot, L. Konate, O. Faye, C. Sokhna, and J.-F. Trape, “Resistance to ddt and pyrethroids and increased kdr mutation frequency in *An. gambiae* after the implementation of permethrin-treated nets in senegal,” *PLoS One*, vol. 7, no. 2, p. e31943, 2012.
- [42] ScienceDaily. (1997, Jul.) Snap! Crackle! Pop! Electric bug zappers are useless for controlling mosquitoes, says UF/IFAS pest expert. [Online]. Available: <http://www.sciencedaily.com/releases/1997/07/970730060806.htm>
- [43] P. Anupa Elizabeth, M. Saravana Mohan, P. Philip Samuel, S. Pandian, and B. Tyagi, “Identification and eradication of mosquito breeding sites using wireless networking and electromechanical technologies,” in *Recent Trends in Information Technology (ICRTIT), 2014 International Conference on*. IEEE, 2014, pp. 1–6.
- [44] B. Hur and W. Eisenstadt, “Low-power wireless climate monitoring system with rfid security access feature for mosquito and pathogen research,” in *Mobile and Secure Services (MOBISERV), 2015 First Conference on*. IEEE, 2015, pp. 1–5.
- [45] J. Ameny, D. Phelps, O. Oladipo, F. Sewovoe-Ekuoe, S. Jadoonanan, S. Jadoonanan, T. Tabassum, S. Gnabode, T. D. Sherpa, M. Falzone, A. Hossain, and

- A. Kublal, “Medizdroids project: Ultra-low cost, low-altitude, affordable and sustainable UAV multicopter drones for mosquito vector control in malaria disease management,” in *IEEE Global Humanitarian Technology Conference (GHTC 2014)*, Oct 2014, pp. 590–596.
- [46] C. Boonsri, S. Sumriddetchkajorn, and P. Buranasiri, “Laser-based mosquito repelling module,” in *Photonics Global Conference (PGC), 2012*. IEEE, 2012, pp. 1–4.
- [47] J. Kare and J. Buffum, “Build your own photonic fence to zap mosquitoes midflight [backwards star wars],” *IEEE Spectrum*, vol. 5, no. 47, pp. 28–33, 2010. [Online]. Available: <http://spectrum.ieee.org/consumer-electronics/gadgets/backyard-star-wars>
- [48] H. Choset, “Coverage for robotics - a survey of recent results,” *Annals of Mathematics and Artificial Intelligence*, vol. 31, no. 1-4, pp. 113–126, October 2001.
- [49] D. Spears, W. Kerr, and W. Spears, “Physics-based robot swarms for coverage problems,” *The international journal of intelligent control and systems*, vol. 11, no. 3, 2006.
- [50] S. Koenig, B. Szymanski, and Y. Liu, “Efficient and inefficient ant coverage methods,” *Annals of Mathematics and Artificial Intelligence*, vol. 31, no. 1, pp. 41–76, Oct. 2001.
- [51] E. M. Arkin, S. P. Fekete, and J. S. B. Mitchell, “Approximation algorithms for lawn mowing and milling,” *Comput. Geom.*, vol. 17, no. 1-2, pp. 25–50, 2000.
- [52] E. M. Arkin, M. A. Bender, E. D. Demaine, S. P. Fekete, J. S. B. Mitchell, and S. Sethia, “Optimal covering tours with turn costs,” *SIAM Journal on Computing*, vol. 35, no. 3, pp. 531–566, 2005.

- [53] M. Gillies and T. Wilkes, “The vertical distribution of some West African mosquitoes (Diptera, Culicidae) over open farmland in a freshwater area of The Gambia,” *Bulletin of entomological research*, vol. 66, no. 01, pp. 5–15, 1976.
- [54] A. T. Becker, M. Debboun, S. P. Fekete, D. Krupke, and A. Nguyen, “Zapping Zika with a mosquito-managing drone: Computing optimal flight patterns with minimum turn cost,” in *32nd Symposium on Computational Geometry (SoCG)*, ser. LIPIcs-Leibniz International Proceedings in Informatics, vol. 77, 2017, pp. 62:1–62:5.
- [55] ardupilot.org. (2016) Motion planner overview. [Online]. Available: <http://ardupilot.org/planner/docs/mission-planner-overview.html>
- [56] S. Bakar, N. Ong, H. Aziz, J. Alcain, W. M. W. N. Haimi, and Z. Sauli, “Underwater detection by using ultrasonic sensor,” in *AIP Conference Proceedings*, 2017.
- [57] S. K. V. Sudarshan and A. T. Becker, “Using gradient descent to optimize paths for sustaining wireless sensor networks,” in *2015 Texas Symposium on Wireless and Microwave Circuits and Systems (WMCS)*, April 2015, pp. 1–6.

